AN ABSTRACT OF THE THESIS OF

Derek A. Tucker for the degree of Honors Baccalaureate of Science in Physics presented on June 4, 2002. Title: Optical Characterization of Transparent Conductive Thin Films.

Abstract approved:

_____

Janet Tate, David McIntyre

The optical characterization of transparent conductive thin films is demonstrated. The basics of transparency and conductivity, as they relate to transparent conductor research, are explained. A functional model of the reflectance and transmittance of a sample film, including interference fringes, is derived from the Fresnel electric field amplitude coefficients. The wavelength-dependent refractive index is determined by analysis of the interference fringes. Two methods for determining the absorption coefficient spectrum have been shown and compared. The absorption coefficient spectrum is used to determine the magnitude and the direct/indirect nature of the energy gap of the material. The significance of the diffuse spectral components of both transmittance and reflectance, with respect to analyzing the energy gap, is also demonstrated

Optical Characterization of Transparent Conductive Thin Films

By

Derek A. Tucker

A PROJECT

Submitted to

Oregon State University

University Honors College

in partial fulfillment of
the requirements for the
degree of

Honors Bachelors of Science in Physics (Honors Associate)

Presented June 4, 2002
Commencement June 2002

Honors Bachelor of Science in Physics project of Derek A. Tucker presented on June 4, 2002.

APPROVED:

_____

Co-Mentor, representing Physics

_____

Co-Mentor, representing Physics

_____

Committee Member, representing Physics

_____

Chair, Department of Physics

_____

Dean, University Honors College

I understand that my project will become part of the permanent collection of Oregon State University, University Honors College. My signature below authorizes release of my project to any reader upon request.

_____

Derek A. Tucker, Author

Acknowledgments

- Dr. Janet Tate, Thesis advisor – For opening many doors, always being there to help, and providing professional and academic advice.

- Dr. David McIntyre, Thesis advisor – For always providing optical theory and technical assistance.

- Dr. Bill Warren – For being part of my thesis defense committee.

- Andrew Draeseke – For providing all of the sample films used in this project.

- Levi Kilcher – For providing some of the spectral data used in the analysis.

- Dr. Tom Plant – For assistance with the Filmetrics spectrometer and for teaching me all about lasers and waveguides.

- Dr. John Wager – For trying to open the door to thin film photovoltaics at OSU.

- Additional thanks to the entire TCO group for always providing support, for creating a great learning environment, and making my research experience at OSU an great one.

TABLE OF CONTENTS

LIST OF FIGURES

LIST OF APPENDICES

LIST OF APPENDIX FIGURES

LIST OF APPENDIX TABLES

Optical Characterization of Transparent Conductive Thin Films

Introduction

Transparent conductor research is all about balancing two mutually exclusive properties of materials, transparency and conductivity. The goal is to create materials that exhibit both of these qualities simultaneously. The challenge is that nature prefers that such things don't occur. To understand this challenge, it will be instructive to consider an idealized energy band model as it relates to both transparency and conductivity.

-Transparency-

The energy band model, used to describe the energy structure of solids, defines the valence band energy level and the conduction band energy level of a material. The difference in energy between the conduction band and the valence band is called the energy band gap (Egap). Figure 1 shows, in terms of these energy bands, how photons interact with a material. When a photon with energy less than Egap is incident on a material, that photon cannot excite an electron from the valence band to the conduction band and simply passes through the material. A material that allows visible photons to pass through in this manner is by definition transparent. In the idealized model, a larger

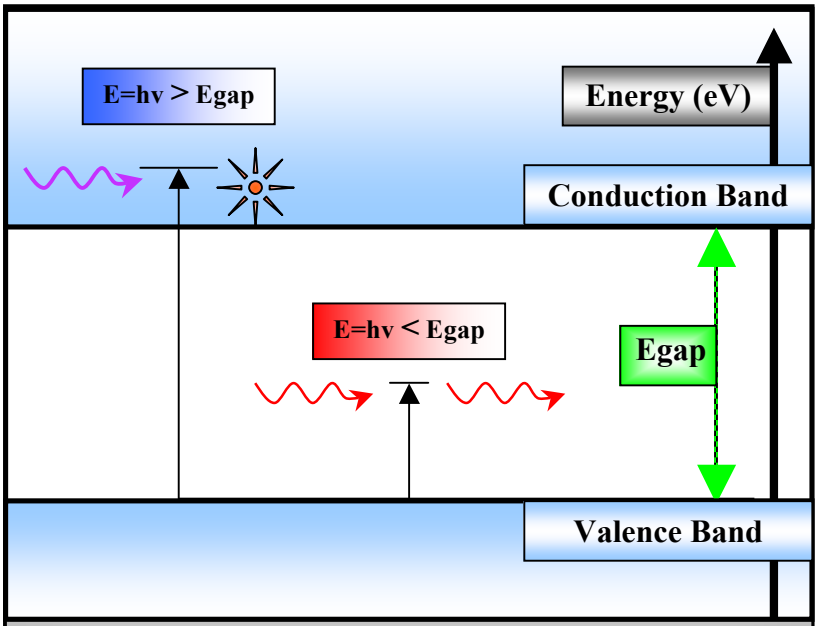

Figure 1: Energy band model - Photon interaction

Egap will allow higher energy photons to pass through without being absorbed resulting in a wider transparency bandwidth. In general, transparent materials will have a large Egap. Common examples of wide-gap insulating materials include SiO_2 (glass) and diamond with Egap values of approximately 8 eV and 5 eV, respectively. Conversely, electronic semiconducting materials like gallium arsenide, silicon, and germanium have Egap values of 1.42 eV, 1.12 eV, and 0.66 eV, respectively. The small magnitude of Egap in these semiconducting materials means that visible photons have more than enough energy to excite electrons across the gap. These photons are therefore readily absorbed and the material is visibly opaque.

When an incident photon has precisely enough energy to excite an electron across the energy band gap, it will again be absorbed by the material through thermal dissipation. In the ideal case, this energy level (Egap) will correspond to an absorption band edge. At lower energies, the ideal transparency is 100% while higher energies are completely absorbed and ideal transparency drops to an opaque 0%. This idealization, shown in Figure 2, presents a useful method of Egap approximation. The transparency versus wavelength spectrum is readily measured experimentally using any number of spectrophotometric devices. Brief analysis of the measured spectrum determines an approximate high-to-low transition wavelength. This allows one to deduce from the idealized model that this transition wavelength, and therefore this photon energy (Appendix A), corresponds to the approximate Egap of the sample material.

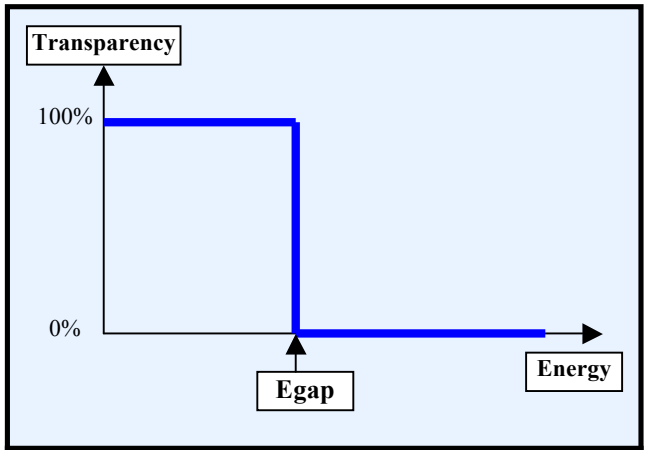

Figure 2: Ideal transparency vs. energy

In practice, transparency does not make a discontinuous jump when the photon energy equals the Egap. Instead, it varies more gradually across this energy region in

correspondence with the absorption coefficient (α), a material dependent factor which has a continuous functional dependence on energy. This absorption coefficient is frequently defined in terms of Beer-Lambert's Law (1),

$$I = I_o\, e^{-\alpha d} \tag{1}$$

a formula that relates transmitted intensity to incident intensity (I_0), given the absorption coefficient (α), and the thickness of the medium (d). From this relation, it is clear that both the absorption coefficient and the thickness of the sample have a great influence on transparency. Thicker films are preferable because of the practical difficulties associated with making very thin films, such as poor adhesion. Therefore, transparent conductors are typically made from wide-gap, low-absorption materials that allow thicker films to be made without compromising transparency. However, these wide-gap transparent materials intrinsically conduct very poorly, if at all. A core motivation behind transparent conductor research is to devise methodology to increase the conductivity of these typically insulating materials to a usable level.

-Conductivity-

Conductivity refers to the conduction, or transport, of charge carriers through a material. The relation between conductivity and a material Egap is again most easily understood in terms of an idealized energy band diagram. Figure 3 shows the natural tendency of electrons to fill the lower energy states of the valence band preferentially over the higher energy conduction band states. When an electron in the valence band is externally excited with enough

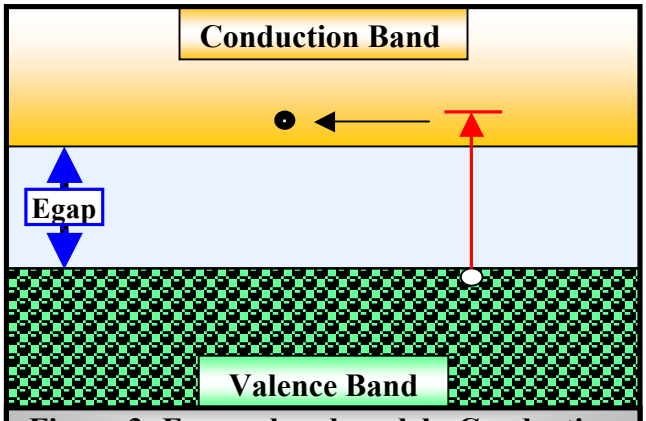

Figure 3: Energy band model - Conduction

energy to break an interatomic bond in the material lattice, it will be excited across the Egap into the sparsely populated conduction band (Fig. 3). This excitation frees the electron to move about the lattice as a charge carrier. Similarly, this excitation opens an empty spot in the valence band, a hole, which serves as a second type of charge carrier in the valence band. In fact, for each electron excited to the conduction band, a hole is opened in the valence band creating an electron-hole pair in the material. The amount of excitation required to create current producing charge carriers in a material, inducing conductivity, is directly proportional to the size of the Egap, or interatomic bond energy.

At low temperatures (near T=0K), the valence band is almost completely filled while the conduction band is nearly empty. In this situation, there are no sites in the material lattice that will accept an electron. The electrons simply move around the lattice with zero net momentum, thereby producing no current, or conductivity of electrons (Pierret, 29). As a result, there are no charge carriers, holes, in the valence band, nor any charge carrying electrons available to inhabit the empty conduction band. The result is that there are no electron-hole pairs created and thus no charge carriers available to induce conductivity at very low temperatures.

As the temperature increases from near zero Kelvin to room temperature, thermal excitation transfers energy to the electrons in the material lattice structure. In materials having a very small Egap, this thermal energy (~ 26-meV) is enough to excite electrons from the valence band into the conduction band and thus induce intrinsic conductivity at room temperature. In fact, in some of the best conductors, the valence band is only partially filled so that even the smallest thermal energy will excite electrons across the intraband Fermi level resulting in conduction of electrons through the available states in the valence band. Conversely, in materials having a wide Egap, this same room temperature thermal energy is insufficient to excite many electrons from the valence band into the conduction band. Thus, small Egap materials have abundant electron-hole pairs available for conduction at room temperature, a characteristic that defines their

classification as conductors. It follows that wide Egap materials have very few electron-hole pairs available for conduction at room temperature and are thereby classified as insulators.

-Solutions-

Having now established the counter-mechanisms of transparency and conductivity, one can more easily see the inherent challenge in achieving both of these qualities simultaneously. Generally speaking, materials with wide energy band gaps are transparent and insulating. Conversely, materials with small energy band gaps are typically opaque and conductive. To overcome this apparent mutual exclusivity of transparency and conductivity, many techniques are employed. The most straightforward method employed to this end is to simply deposit these materials as thin films on transparent substrates. Recalling equation (1), a thinner film decreases the path length that a photon must travel in a material, thereby reducing the attenuation of the transmitted intensity. Typically, these thin films are a few hundred nanometers thick, which is on the same order of magnitude as a wavelength of visible light (as such, thin film interference effects cannot be ignored). However, very thin films are difficult to produce and tend to be fragile. Also, a very thin film is not versatile enough for practical application to microelectronics so simply decreasing the thickness of a conductor is not a viable solution.

A different and more involved approach is to add impurities, or dopants, to the material during deposition. The addition of impurity sites to the material lattice structure is a method of controllably altering the conductivity of a material by introducing a specific type of carrier, electrons or holes, without appreciably affecting the other type. This is accomplished by introducing a dopant that has either one more valence electron per atom, or one less valence electron per atom, than the atoms of the base material. In terms of the energy band model, these impurity site energy levels lie between the valence

band and the conduction band, within the Egap. In Figure 4, introduced impurities have created excess electrons. At near zero Kelvin, these electrons occupy the impurity (donor) sites just below the conduction band. In silicon, for example, these impurity sites would lie ~ 40-meV below the conduction band. At room temperature (~ 26-meV), there is now enough thermal energy present to excite, or donate, electrons into the conduction band. More precisely stated, with the Fermi level now positioned in the narrow region between the impurity sites and the conduction band, the curved transition tail in the Fermi-Dirac occupation probability function, at room temperature, will now penetrate the conduction band. As a result, there is a reasonable probability that electrons will occupy the conduction band at room temperature (as shown in the right side of Figure 4). As previously discussed, these conduction electrons are now free to contribute to the conductivity of the material. For the analogous case of excess holes in the valence band, empty impurity (acceptor) sites are located just above the valence band at near zero Kelvin. At room temperature, there is enough thermal energy to excite electrons into these acceptor sites leaving holes open in the valence band where they can now act as charge carriers.

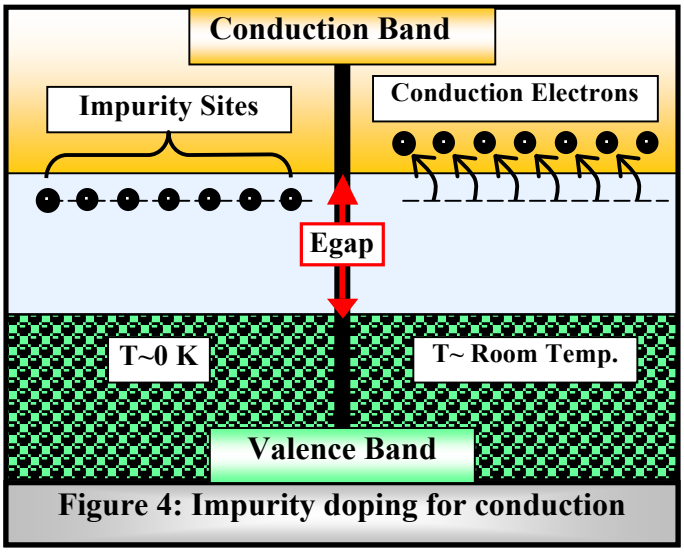

Figure 4: Impurity doping for conduction

In the language of solid state electronics, doping creates n-type or p-type materials depending on the nature of the impurity in relation to the base material. When excess electrons are created in the conduction band, the material is called n-type. Conversely, when excess holes are created in the valence band, the material is called p-type. These materials are at the core of all solid state electronics today in the form of n- and p-type silicon. Since there are already well-understood n-type transparent conductors, such as

indium tin oxide, most transparent conductor research today is focused on developing p-type materials. Once both types of well-characterized transparent materials are available, many new technologies will be possible. As one example, combining optical waveguide technology with traditional "2-D" microelectronic circuitry may bring to fruition new "3-D" integrated circuit design techniques.

Optical Characterization

-Overview-

When pursuing the optical characterization of a transparent conductive thin film, one seeks to determine all relevant optical properties, some surface quality properties, and the magnitude and nature of the energy band gap of the material. A typical starting point is to measure the thickness of the film mechanically with a profilometer. Next, the transparency and reflectivity are measured as a function of wavelength. Figure 5 shows

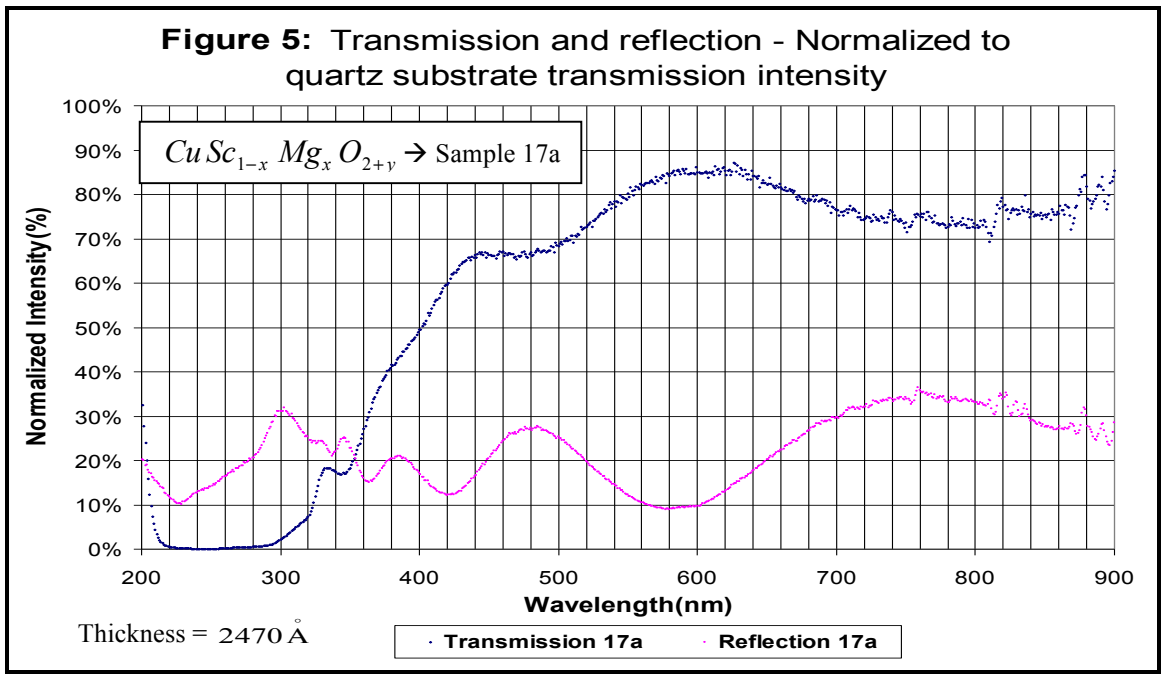

an example of these measurements taken for a sample tagged 17a, one of a series of films made with different oxygen intercalation pressures. From this spectral data one quickly sees that this particular film has an average transparency of about 75% across most of the visible spectrum (~ 450nm-700nm), while the reflectivity maintains an average of about 20% across the entire measured spectrum. It should be noted that the drop in transparency, at the shorter wavelengths in Figure 5, is due to these higher energy photons being absorbed by the material, as discussed earlier. Conversely, the reflectivity

does not fall off at these lower wavelengths because the beam reflected from the face of the sample never enters the material and therefore never encounters the absorbing medium.

The most striking feature of Figure 5 is the sinusoidal appearance of the spectral data. This variation in intensity is due to thin film interference, which arises from the path-length difference of light reflecting from the front and back surfaces of the film. This effect is apparent in both transmission and reflection, where transmission maxima are aligned with reflection minima and vice versa. These interference fringes provide a useful method for determining the index of refraction of the film. After constructing a formula for optical path length difference, Eqn. (13), one relates the associated phase difference to the appropriate condition for constructive interference (intensity maxima) or destructive interference (intensity minima). Such a formulation can then be used to determine the refractive index at discrete wavelengths corresponding to the associated intensity maxima and minima.

When one seeks the absorption coefficient, the interference fringes introduce error into the solution. Here, the reflection spectrum is the key to minimizing this error. Noting again that if angles of incidence are identical, the reflection maxima are aligned with transmission minima and one can use the reflection spectrum to cancel the fringes in the transmission spectrum. The resulting "fringe-free" transmission spectrum can then be used, via Beer-Lambert's Law, to determine the "improved" absorption coefficient (α), which quickly indicates the magnitude of the energy band gap when plotted as a function of energy. With some additional analysis, the absorption coefficient can be helpful in determining whether the material has a direct or indirect energy band gap.

Aside from the interference fringes, there is still structure that remains in the spectral data. One source of this remaining structure is scattering. As an incident beam of light encounters a non-ideal, inhomogeneous material, photons will be scattered by surface roughness and material impurities or inclusions. By measuring the scattered, or diffuse,

intensities in reflection and transmission, one can gain insight into the relative surface roughness and potentially even the grain size of the deposited material.

In practice, measuring the transparency and reflectivity of a thin film sample can be accomplished in many ways. The fastest method uses a diode-array spectrometer, which measures the transmitted or reflected intensity across the entire visible spectrum simultaneously. A broad band "white light" source is incident on a material and the transmitted or reflected beam is dispersed by a grating onto an array of photodiodes, each of which therefore measures the response at a different wavelength. A down side to such devices, and many other spectrometers as well, is that they often measure only a narrow spectral range (from 400nm to 800nm). In characterizing transparent conductors, the absorption transition region typically lies in the ultraviolet portion of the electromagnetic spectrum, just below the lower limit of common visible light spectrometers. Additionally, the intrusive software these "push-button" spectrometers use can sometimes prevent easy access to the raw data while it tries to calculate, with only marginal success, all of the optical properties of the sample. However, if one seeks only a quick comparison of the overall transparency, a diode-array spectrometer is by far a more convenient tool.

The alternative to the diode-array spectrometer is the scanning spectrometer. This sort of system uses a lamp in series with a wavelength dispersive element to achieve an approximately monochromatic output. This output passes through a series of lenses and mirrors such that the incident spot size of the focused beam is smaller than the size of the film sample. The incident beam is then reflected or transmitted onto the face of a silicon photodetector. Using a simple computer interface, the output can be scanned over a range of wavelengths by changing the angle of the monochromator diffraction gratings. To build the intensity spectrum, the computer saves a power reading from the photodetector at each of these wavelengths. This data is then easily manipulated in a spreadsheet program. The greatest advantage to such a system is that it can be readily

modified to suit the needs of the investigation. For example, the detector can be placed close to the film sample to capture all the transmitted or reflected light, or it can be moved farther away (and an optional iris inserted) to capture only directly transmitted or reflected light while much of the scattered light escapes. Also, with the sample placed after the dispersive element, the incident wavelength may cause photoluminescence in the film, which will be recorded as additional intensity at the incident wavelength. To avoid this, the sample can be mounted before the dispersive element such that the photoluminescent output is "filtered out" as it is dispersed out of the measured wavelength. This kind of system was employed for the collection of all the data shown in this paper. In this case, the lamp, the diffraction gratings, the mirrors, the lenses, and the photodetector were all chosen to maximize the output in the vital ultraviolet region of the spectrum. Appendix B includes an extensive description of this system.

-Transmittance and Reflectance-

To fully understand the optical characteristics of a sample material, one must start with the Fresnel coefficients, mathematical formulations that are used to define the amplitude of the reflected and transmitted portions of the electric field (**E**) component of the incident electromagnetic wave (Hecht, 112). These coefficients are defined with respect to the plane of incidence, which is the plane containing both the incident and reflected beam. When the **E**-field is perpendicular to the plane of incidence, the amplitude reflection and transmission coefficients are

$$r_{\perp} = \left(\frac{n_i \cos\theta_i - n_t \cos\theta_t}{n_i \cos\theta_i + n_t \cos\theta_t} \right) \qquad t_{\perp} = \left(\frac{2 n_i \cos\theta_i}{n_i \cos\theta_i + n_t \cos\theta_t} \right) \tag{2}$$

Similarly, when the **E**-field is parallel to the plane of incidence, the amplitude reflection and transmission coefficients are

$$r_{//} = \left(\frac{n_t \cos\theta_i - n_i \cos\theta_t}{n_i \cos\theta_t + n_t \cos\theta_i} \right) \qquad t_{//} = \left(\frac{2 n_i \cos\theta_i}{n_i \cos\theta_t + n_t \cos\theta_i} \right) \tag{3}$$

where θ_i, n_i and θ_t, n_t are the angle (relative to the normal) and refractive index of the incident and transmitted beams, respectively. However, one actually measures intensity, not **E**-field amplitude, when measuring transmission and reflection spectra. The intensity coefficients, reflectance ***R*** and transmittance ***T***, are defined as the square of their respective amplitude coefficients, except that the transmittance must include an extra factor to compensate for the different speed of energy transport in the incident and transmitted media (Hecht, 119).

$$R_{\perp} = r_{\perp}^2 \qquad R_{//} = r_{//}^2 \qquad T_{\perp} = \left(\frac{n_t \cos\theta_t}{n_i \cos\theta_i}\right) t_{\perp}^2 \qquad T_{//} = \left(\frac{n_t \cos\theta_t}{n_i \cos\theta_i}\right) t_{//}^2 \tag{4}$$

When $\theta_i = 0^{\circ}$, the perpendicular and parallel components are indistinguishable and *R* and *T* are considerably simplified, that is,

$$R = R_{//} = R_{\perp} = \left(\frac{n_t - n_i}{n_t + n_i}\right)^2 \qquad T = T_{//} = T_{\perp} = \left(\frac{4\, n_t n_i}{\left(n_t + n_i\right)^2}\right) \tag{5}$$

How to average the coefficients for non-normal incidence of randomly polarized light was not considered. To make use of the Fresnel coefficients, each material interface is assigned its respective *R* and *T* coefficients. As an incident beam of intensity $\left(I_0\right)$ encounters each interface, the reflected and transmitted intensity components, which take no account of interference fringes, are $\left(R\, I_0\right)$ and $\left(T\, I_0\right)$ respectively. Combining these components with Beer-Lambert's Law, equation (1), allows a multiple ray bounce analysis of any multi-layer planar optical system. Figure 6 shows the simplified, first-order (only a single bounce at each interface) ray bounce diagrams for a thin film on a substrate and also for an isolated substrate. Here, each reflected or transmitted beam is assigned a functional value, such that the total reflected or transmitted intensity may be calculated. For the air-film-substrate-air structure, the first-order transmitted and reflected intensity, normalized to the incident intensity $\left(I_0\right)$, is

$$T_{Film-Substrate} = \frac{I_0 D}{I_0} = \frac{I_0 \left(T_{AF} T_{FS} T_{SA} e^{-\alpha d} \right)}{I_0} = T_{AF} T_{FS} T_{SA} e^{-\alpha d} \quad (6)$$

$$R_{Film-Substrate} = \frac{I_0 (A + B + C)}{I_0} = R_{AF} + T_{AF}^2 R_{FS} e^{-2\alpha d} + T_{AF}^2 T_{FS}^2 R_{SA} e^{-2\alpha d} \quad (7)$$

where it is assumed that no absorption ($\alpha = 0$) occurs in the substrate. It is useful to characterize the substrate in the same manner, as any anomalous substrate spectral

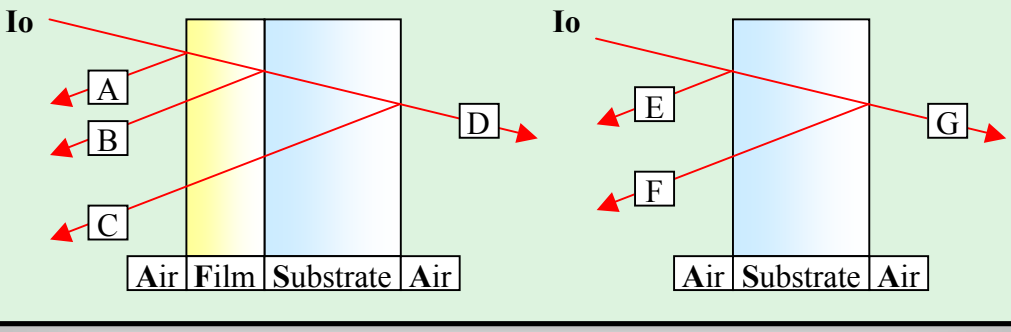

Figure 6: First-order ray bounce diagrams for single and multi-layer structures

structure could be mistaken for a film characteristic and thereby introduce error into the film analysis. Since the refractive index of fused silica, or fused quartz, is well known, a numerical value for substrate transmission and reflection over the visible spectrum can be calculated as

$$T_{Substrate} = \frac{I_0 G}{I_0} = \frac{I_0 T_{AS} T_{SA}}{I_0} = T_{AS} T_{SA} = 92.16\% \quad (8)$$

$$R_{Substrate} = \frac{I_0 (E + F)}{I_0} = \frac{I_0 \left(R_{AS} + T_{AS}{}^2 R_{SA} \right)}{I_0} = \left(R_{AS} + T_{AS}{}^2 R_{SA} \right) = 7.68\% \quad (9)$$

where $n_{Air} = 1.0$, $n_{Substrate} \approx 1.5$, $\alpha = 0$, and $\theta_i = 0^\circ$.

While the first-order approximation of Figure 6 is illustrative, the infinite bounces that occur along the path of each ray must be accounted for as well (Peyghambarian, 67). To reduce complexity, while introducing an error of just a percent or so, only a single

bounce at the back surface of the glass is considered. The equation for total fringe-free transmission through a film-substrate structure is

$$T_{Film-Substrate} = T_{AF}T_{FS}T_{SA}e^{-\alpha d}\left[1 + R_{AF}R_{FS}e^{-2\alpha d} + R_{AF}^2R_{FS}^2e^{-4\alpha d} + \ldots\right] = \frac{\left(T_{AF}T_{FS}T_{SA}e^{-\alpha d}\right)}{1 - R_{AF}R_{FS}e^{-2\alpha d}} \qquad (10)$$

where the bracketed [ ] term is a convergent geometric series representing the infinite internal bounces that occur within the film. Here it is assumed that the substrate has no absorption. Using the same assumptions, the equation for total fringe-free reflection is

$$R_{Film-Substrate} = R_{AF} + T_{AF}^2R_{FS}e^{-2\alpha d}\left[\frac{1}{1 - R_{AF}R_{FS}e^{-2\alpha d}}\right] \qquad (11)$$

where the bracketed [ ] term is again a convergent geometric series that represents the infinite internal bounces within the film.

To this point, the interference fringes found in real spectral data have not been accounted for. The inclusion of interference fringes requires a more exacting treatment of reflectance and transmittance in terms of the **E**-field amplitude coefficients because, unlike the intensity coefficients, they retain the phase information that defines the interference pattern (Hecht, 411). This phase shifting arises from the optical path length difference between adjacent beams and also from the sign $(\pm)$ of the amplitude coefficients. Referring to the model in Figure 7, the optical path length difference is constructed as

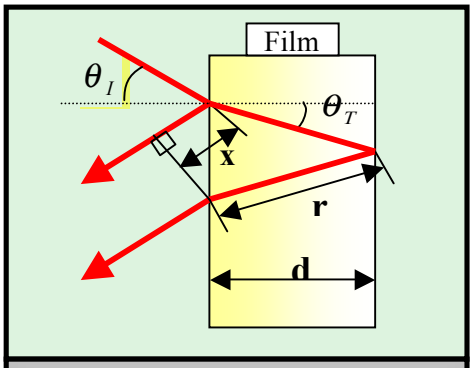

Figure 7: Geometric path length difference between adjacent reflected beams

$$\Lambda = 2r\,n_{film} - x\,n_{air} = \frac{2d\,n_{film}}{\cos\theta_T} - \frac{2d\,n_{air}}{\cos\theta_T}\left(\sin\theta_T \sin\theta_I\right) \qquad (12)$$

where the associated phase difference is found to be

$$\delta = k_o \Lambda = k_o 2r - k_o x = \left(\frac{4\pi d}{\lambda_0 \cos\theta_T}\right)\left(n_{film} - \sin\theta_T \sin\theta_I\right) \tag{13}$$

such that δ is the single round-trip phase difference due only to the physical distance traveled through the film. This phase difference can be further simplified with Snell's Law $\left(n_1 \sin\theta_1 = n_2 \sin\theta_2\right)$and a trigonometric identity $\left(1 - \sin^2\theta_T = \cos^2\theta_T\right)$as

$$\delta = \left(\frac{4\pi d}{\lambda_0 \cos\theta_T}\right)\left(n_{film} - \sin\theta_T\left(n_{film}\sin\theta_T\right)\right) = \left(\frac{4\pi d\, n_{film}}{\lambda_0 \cos\theta_T}\right)\left(1 - \sin^2\theta_T\right) = \left(\frac{4\pi d\, n_{film}}{\lambda_0}\right)\cos\theta_T \tag{14}$$

As long as the amplitude coefficients, equations (2) and (3), and the path-length dependent phase difference, equation (14), are carefully applied, the total reflected and transmitted **E**-field amplitude coefficients are derived in precisely the same manner as equations (10) and (11), the total intensity coefficients. These amplitude coefficients can then be converted to "phase accurate" intensity coefficients by taking the complex square of their magnitudes (Schroder, 605). However, when considering interference effects it's legitimate to ignore the beams reflecting off the back surface of the substrate. Since the coherence length of "white" light is just a few micrometers and the thickness of the substrate is a millimeter or so, the phases of the photons reaching the back surface of the substrate have become random. When these randomly phased photons interfere, the net effect averages to zero. The resulting intensity coefficients, including interference fringes, are found as

$$R = \left|-r_{AF} + \frac{t_{AF} r_{FS} t_{FA} e^{-i\delta} e^{-\alpha\left(d/\cos\theta_T\right)}}{1 - r_{AF} r_{FS} e^{-i\delta} e^{-\alpha\left(d/\cos\theta_T\right)}}\right|^2 = \frac{r_{AF}^2 + r_{FS}^2 e^{-\alpha\left(2d/\cos\theta_T\right)} - 2 r_{AF} r_{FS} e^{-\alpha\left(d/\cos\theta_T\right)}\cos\delta}{1 + r_{AF}^2 r_{FS}^2 e^{-\alpha\left(2d/\cos\theta_T\right)} - 2 r_{AF} r_{FS} e^{-\alpha\left(d/\cos\theta_T\right)}\cos\delta} \tag{15}$$

$$T = \left|\frac{t_{AF} t_{FS} t_{SA} e^{-\alpha\left(d/2\cos\theta_T\right)}}{1 - r_{AF} r_{FS} e^{-i\delta} e^{-\alpha\left(d/\cos\theta_T\right)}}\right|^2 = \frac{t_{AF}^2 t_{FS}^2 t_{SA}^2 e^{-\alpha\left(d/\cos\theta_T\right)}}{1 + r_{AF}^2 r_{FS}^2 e^{-\alpha\left(2d/\cos\theta_T\right)} - 2 r_{AF} r_{FS} e^{-\alpha\left(d/\cos\theta_T\right)}\cos\delta} \tag{16}$$

In the calculations for **R** and **T**, there is a 180° phase shift included in the reflected amplitudes that arises when the incident beam encounters a low-to-high index interface. Here also, the absorption term includes $(d/\cos\theta_T)$, which compensates for the increased

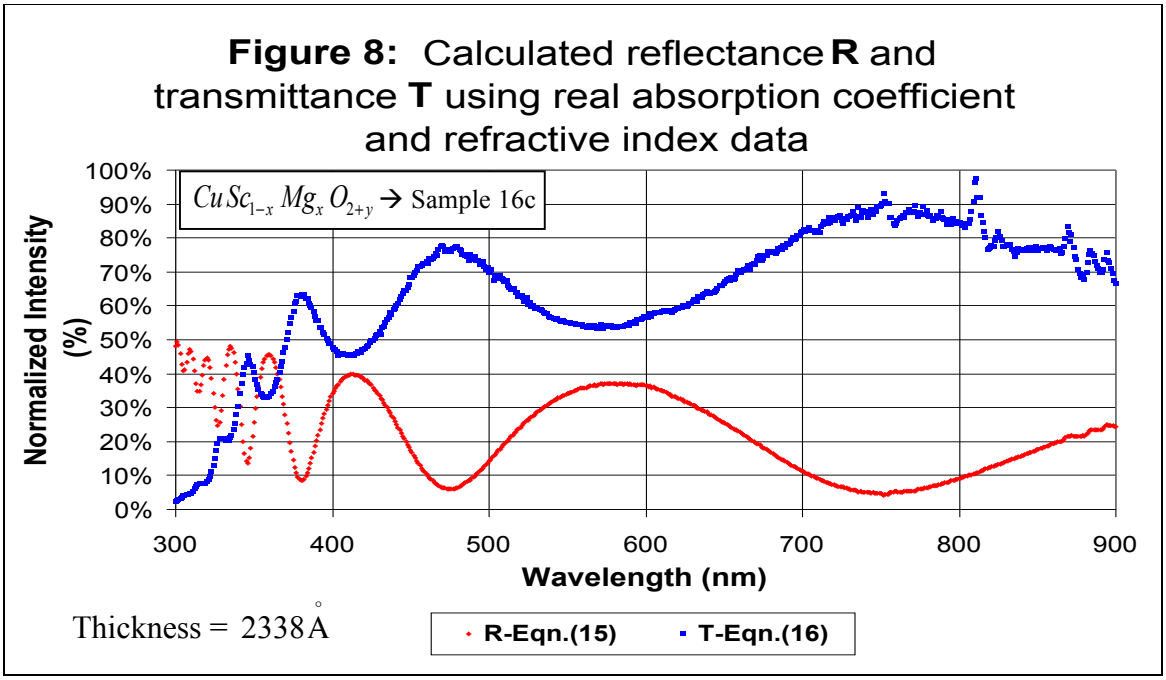

path length that arises at angles other than normal incidence. Figure 8 shows a plot of equations (15) and (16) using the index of refraction and absorption coefficient determined for the film tagged SM-16c, another in the series of oxygen intercalated copper scandium oxide films referenced earlier.

Equations (15) and (16) contain all of the relevant variables needed to complete an optical characterization of a thin film on a transparent substrate. The next step is to use the experimentally measured spectral data to extract real values that can be assigned to these variables, which describe the optical properties of the sample material.

Experimental Analysis

To start the optical characterization, one first measures a lamp spectrum, a blank substrate transmission spectrum, and then the reflectance and transmittance spectra for the film-on-substrate structure. From these data alone, nearly all of the unknowns of equations (15) and (16) can be extracted. These unknowns include the refractive indices of the materials, the absorption coefficient (α) of the film, the thickness (d) of the film, and the incident angle of the beam of light. The incident angle is simply noted during measurement. The thickness is typically measured mechanically with a profilometer. The refractive index of the substrate, usually fused quartz, is well known and can be taken from published data. However, the refractive indices of the films being created are not known. Thus, all that now remains to be found is the absorption coefficient and refractive index of the film.

-Refractive Index-

While the refractive index of a material is often quoted as constant, an accurate quantitative analysis requires using the wavelength-dependent index of refraction. As mentioned previously, the refractive index of a thin film can be derived using the interference fringes present in the normalized reflectance and transmittance spectra. In practice, it is more convenient to use only the reflection fringes. The strong absorption seen in transmission is absent in reflection. Thus the reflection fringes are more distinct in this region and allow more accurate determination of the maxima and minima. Using the formula for the path-length dependent phase difference, Eqn. (14), with the addition of a $(\pm\pi)$ phase shift that occurs, in reflection, at the front face of the film,

$$\delta = \left(\frac{4\pi d n}{\lambda_0}\right)\left(\cos\theta_T\right) \pm \pi \qquad (17)$$

one applies the appropriate condition for constructive or destructive interference

$$\delta = 2\pi m(\,for\ \max ima) \qquad \delta = 2\pi(m+\tfrac{1}{2})\,(\,for\ \min ima) \qquad (18)$$

so that the wavelength dependent refractive index can be calculated at each specific wavelength that corresponds to an interference fringe maximum or minimum.

In order to proceed, equations (17) and (18) are solved for λ_{MAX} and λ_{MIN} using Snell's Law to calculate the angle (θ_T) of the beam transmitted into the film, such that

$$\lambda_{MAX} = \frac{2nd}{m+\frac{1}{2}}\left(\cos\left[\sin^{-1}\left(\frac{\sin\theta_I}{n}\right)\right]\right) \qquad \lambda_{MIN} = \frac{2nd}{m}\left(\cos\left[\sin^{-1}\left(\frac{\sin\theta_I}{n}\right)\right]\right) \qquad (19)$$

can be used to construct convenient tables, where the values of the refractive index and the order (m) of the fringes can be cross-referenced to match the experimentally determined maxima and minima wavelength points. It is then a trivial matter to read off the discrete values of the refractive index from these tables. Figure 9 shows the results of such a derivation, the details of which can be found in Appendix C.

Figure 9: Calculated refractive index - Film and substrate

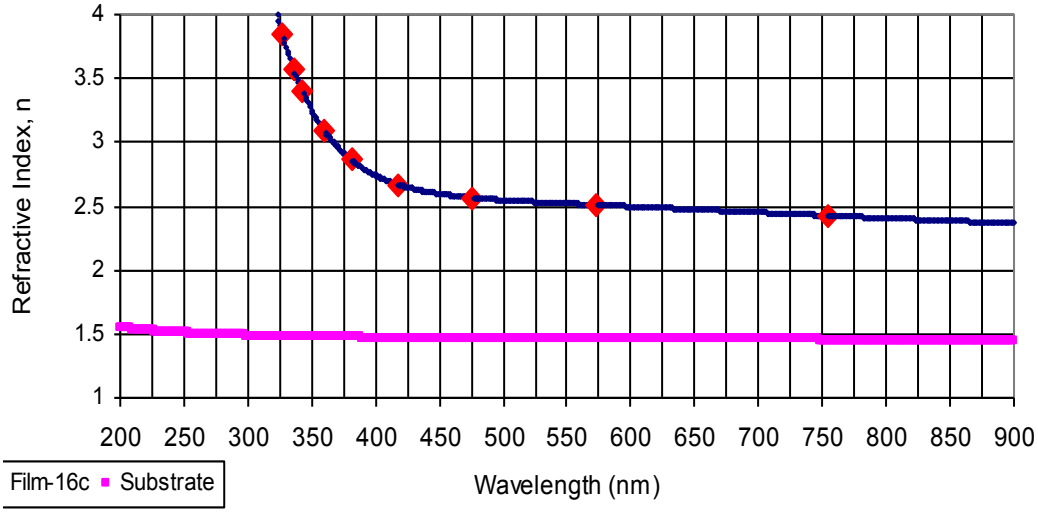

The two curves in Figure 9 correspond to the wavelength dependent refractive indices for the film sample and the fused silica substrate. The fused silica substrate is a well-characterized material so the index curve was simply taken from published data (Driscoll,

1978). The nearly constant refractive index of the fused silica substrate is indicative of a highly transparent wide-Egap material. Its region of absorption falls well outside the visible spectrum. By contrast, the index curve of the thin film sample shows a sharp increase around 400nm indicating a strong absorption band in the near-UV region of the spectrum. This sort of characteristic is common with transparent conductors because an Egap of approximately 3 eV or higher is necessary to prevent heavy absorption in the visible region of the spectrum.

-Absorption Coefficient-

It has been common practice to use only the normalized transmission spectrum of a sample to determine the absorption coefficient with Beer-Lambert's Law, equation (1).

$$I = I_0 e^{-\alpha d} \Rightarrow T = e^{-\alpha d} \xrightarrow{\text{Solve For } \alpha} \alpha = \left(-1/d\right)\ln(T) \tag{20}$$

However, the interference fringes present in such a spectrum are transferred into the derived absorption coefficient spectrum. To negate these unwanted ambiguities, both the reflectance and transmittance must be used to calculate a fringe free transmission spectrum (Hishikawa, 1009). With only the measured **R** and **T** spectra, and a measured film thickness, a simple application of Beer-Lambert's Law can be used to derive an improved "fringe free" absorption coefficient spectra.

Consider a single layer film in air and assume that $(R+T+A=1)$, where R is reflectance, T is transmittance, and A is the intensity that is absorbed in the film. The incident beam is partially reflected at the surface of the film and immediately beyond this interface, the intensity of the beam is $(1-R)$. This can be equivalently thought of as $(T+A)$, where the intensity is made up of that which will be transmitted through the film and that which will be absorbed during its passage through the film. Since Beer-Lambert's Law describes the absorption of light traveling through a medium, this quantity serves as the new (I_o). As the beam now travels through to the rear inner face

of the film, it is absorbed according to $\left(e^{-\alpha d}\right)$. Since the quantity (A) is the absorbed portion, all that remains as the beam reaches the rear inner face is (T), which is now equal to the new beam intensity (I). Using the model just described, these quantities are simply plugged in to equation (1). The result of this derivation is shown in equation (21) as:

Thickness = 2338 Å

$$\left(\frac{T}{1-R}\right) = e^{-\alpha d} \xrightarrow{\text{Solve For } \alpha} \alpha = \left(-1/d\right)\ln\left(\frac{T}{1-R}\right) \tag{21}$$

It must be noted that this method, while simple, accounts only for the beam's travel up to the second interface. Neglected are the transmittance through the rear film-air interface and the multiple internal reflections that occur at this interface. Figure 10 shows the calculated "fringe free" transmittance in comparison to the experimentally measured **R** and **T**. The $\left(\mathbf{T/1-R}\right)$ curve has almost no fringe structure.

Figure 10: Calculated "fringe free" transmission using R and T

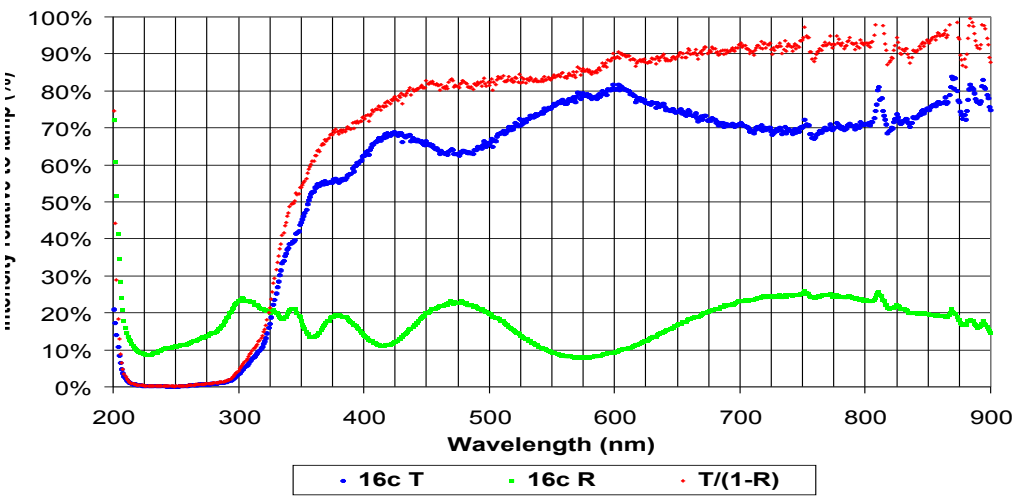

Despite this improvement, analyzing the functional form of **T** and **R** in equations (15) and (16) reveals a missing scale factor, that must be included before (α) is calculated. As noted above, and by inspection of equation (22), one finds that this scale factor arises from the loss of intensity due to infinite "absorbing" passes and associated reflections at

the film-substrate interface. To this point, all of these losses have been included in the absorption coefficient calculation but this calculation should involve only a single pass through the film. The result of this oversight is an artificially high absorption coefficient when using the simple model.

The derivation of this corrective factor is carried out in a straightforward manner by substitution of equation (15) and (16) in the equation for the fringe free transmission.

$$\left(\frac{\mathbf{T}}{1-\mathbf{R}}\right)=\frac{\left(\frac{\left(1-r_{AF}^2\right)\left(1-r_{FS}^2\right)\chi}{1+r_{AF}^2\,r_{FS}^2\,\chi^2-2r_{AF}\,r_{FS}\,\chi\cos\delta}\right)}{\left(\frac{1-r_{AF}^2+r_{FS}^2\,\chi^2\left(r_{AF}^2-1\right)}{1+r_{AF}^2\,r_{FS}^2\,\chi^2-2r_{AF}\,r_{FS}\,\chi\cos\delta}\right)}=\frac{\left(1-r_{AF}^2\right)\left(1-r_{FS}^2\right)\chi}{\left(1-r_{AF}^2\right)\left(1-r_{FS}^2\,\chi^2\right)}=\frac{\left(1-r_{FS}^2\right)\chi}{\left(1-r_{FS}^2\,\chi^2\right)} \quad (22)$$

where $\chi=e^{-\alpha\left(d/\cos\theta_T\right)}$ and $t_{(\,)}^2=\left(1-r_{(\,)}^2\right)$ and r_{FS}^2 can be replaced by R_{FS}, the intensity coefficient at the film-substrate interface. Solving the quadratic equation (22) for χ allows the derivation of the corrected, complete absorption coefficient, which is given by

$$\alpha=\left(\frac{-\cos\theta_T}{d}\right)\ln\left[\frac{-\left(1-R_{FS}\right)+\sqrt{\left(1-R_{FS}\right)^2+\left(\frac{4R_{FS}T^2}{(1-R)^2}\right)}}{2R_{FS}\left(\frac{T}{1-R}\right)}\right] \quad (23)$$

This correction introduces significant complexity to the solution, but the resulting absorption coefficient has a magnitude that appropriately represents the level of absorption in the film.

In practice, when analyzing a large number of similar films, it may be useful to first employ the more accurate, complex method to determine the appropriate scale factor for a given material system and then use this to correct the absorption coefficient spectra determined using the simple method. This sort of correction is possible because the scale factor is relatively constant over the entire region of the spectrum for which reliable data

has been collected. Figure 11 is a comparison of these two methods, equation (21) and

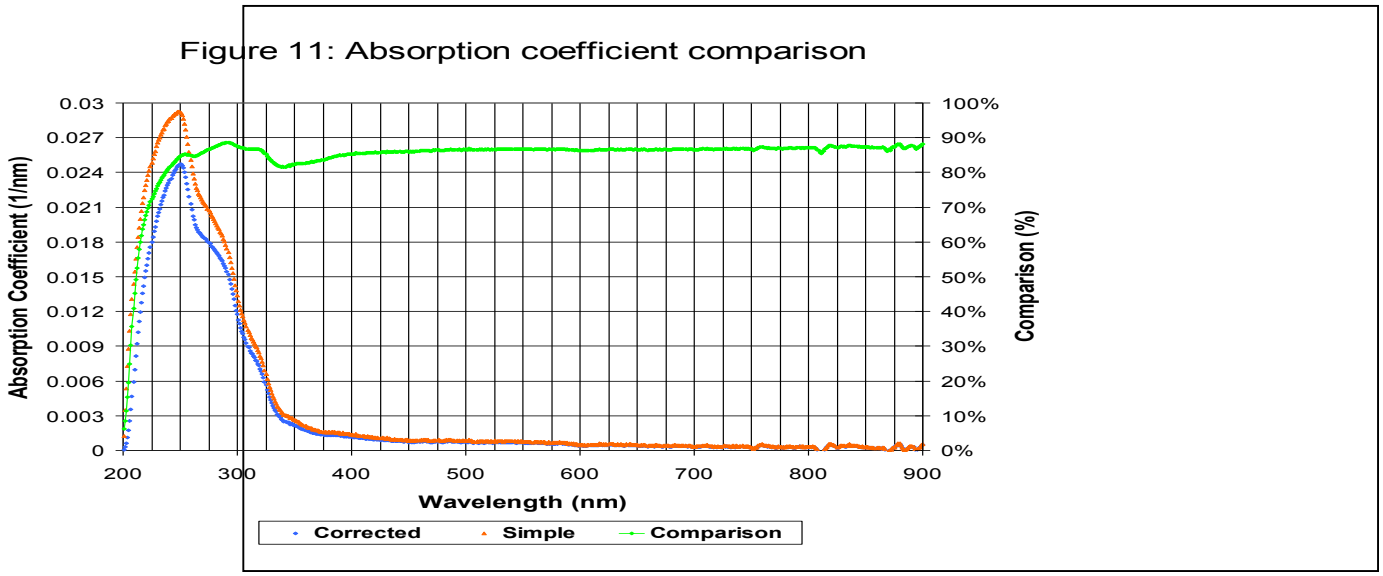

(23), showing that equation (21), the simple version, is artificial enlarged due to the exclusion of rear-interface transmittance and multiple internal reflections.

-Energy Gap Analysis-

When performing a band gap analysis, one plots the absorption coefficient versus energy, rather than wavelength. The conversion is simple and is described in Appendix A. Figure 12 shows the resulting absorption coefficient versus energy spectra. Included

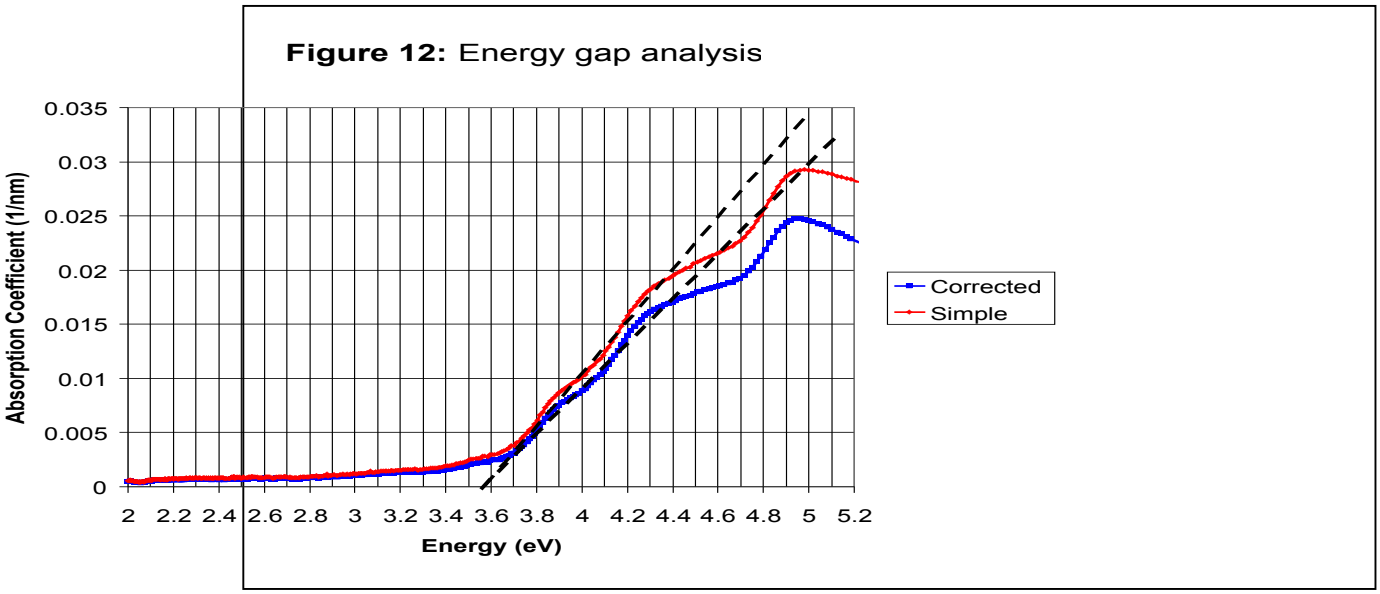

in these plots are the linear approximations used to estimate the energy gap of the material. The energy value at the point where the linear approximation intersects the zero-absorption axis is Egap. Thus, the gap energy can be read directly off the horizontal axis of the plot. Here it is clear that both the simple and complex absorption spectra give a very similar Egap value (~ 3.55-eV), despite the difference in magnitudes. Thus, if only the Egap of a material is being sought and the magnitude of the absorption coefficient is not being considered, the simple formulation is sufficient to obtain an accurate Egap approximation.

The absorption coefficient can also be used investigate the direct/indirect nature of the energy gap. There are three types of gap transitions—direct, indirect, and forbidden direct (Pankove, 34). Each type of transition induces a characteristic shape in the absorption coefficient spectrum. To determine the type of gap transitions that occur in a material, one attempts to linearize the absorption coefficient data by plotting it to the appropriate inverse exponential power.

The absorption coefficient in a material with a direct gap transition is:

$$\alpha(h\nu) \propto \left(h\nu - E_{gap}\right)^{1/2} \tag{24}$$

For indirect gap transitions, the absorption coefficient is proportional to:

$$\alpha(h\nu) \propto \left(h\nu - E_{gap}\right)^{2} \tag{25}$$

Finally, for forbidden direct transitions, the absorption coefficient is:

$$\alpha(h\nu) \propto \left(\frac{1}{h\nu}\right)\left(h\nu - E_{gap}\right)^{3/2} \tag{26}$$

To linearize the theoretical equations for each type of transition, the absorption coefficient spectrum must be plotted as $(\alpha E)^2$ vs. E for direct gaps, as $(\alpha E)^{1/2}$ vs. E for indirect gaps, and as $(\alpha E^2)^{2/3}$ vs E for forbidden direct gap transitions. To determine the type of transition represented by the experimentally determined absorption coefficient,

each of these must be plotted to allow a comparison of their linearity. Due to the nature of the experimental data, this is an unfailingly ambiguous procedure. The analysis in

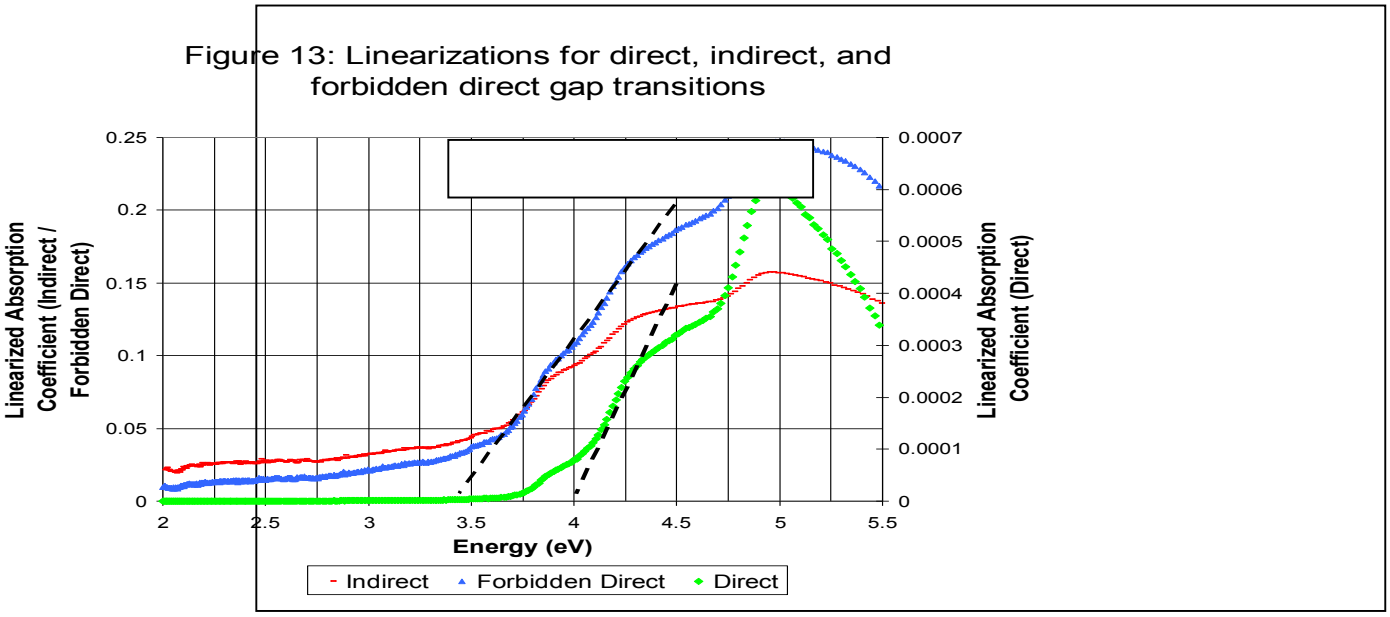

Figure 13 shows that this material is likely a direct or forbidden direct gap material.

Thickness = 2338 Å -Scattering-

To this point, all emphasis has been on direct transmission and reflection measurements. However, a significant amount of light is scattered in some manner as it encounters the sample. Every interface has a certain roughness associated with its surface. This surface roughness scatters, or diffuses, the incident beam of light. Related to surface roughness are the grain boundaries that form as a material is deposited. They define the boundaries of the "bumps" on the surface. Other scattering mechanisms include the presence of lattice impurities, small variations in the refractive index, and also small variations in the density of the film.

To clearly see the influence of scattering, one must investigate the difference in transmission spectra that result from two measurement techniques devised to include or exclude the scattered portion of the transmitted beam. To gather all of the scattered light, the detector was placed very close to the backside of the sample. Conversely, to exclude

much of the scattered light, the detector was placed far from the sample and an adjustable iris was inserted, adjacent to the detector, in the path of the exiting beam. Figure 14

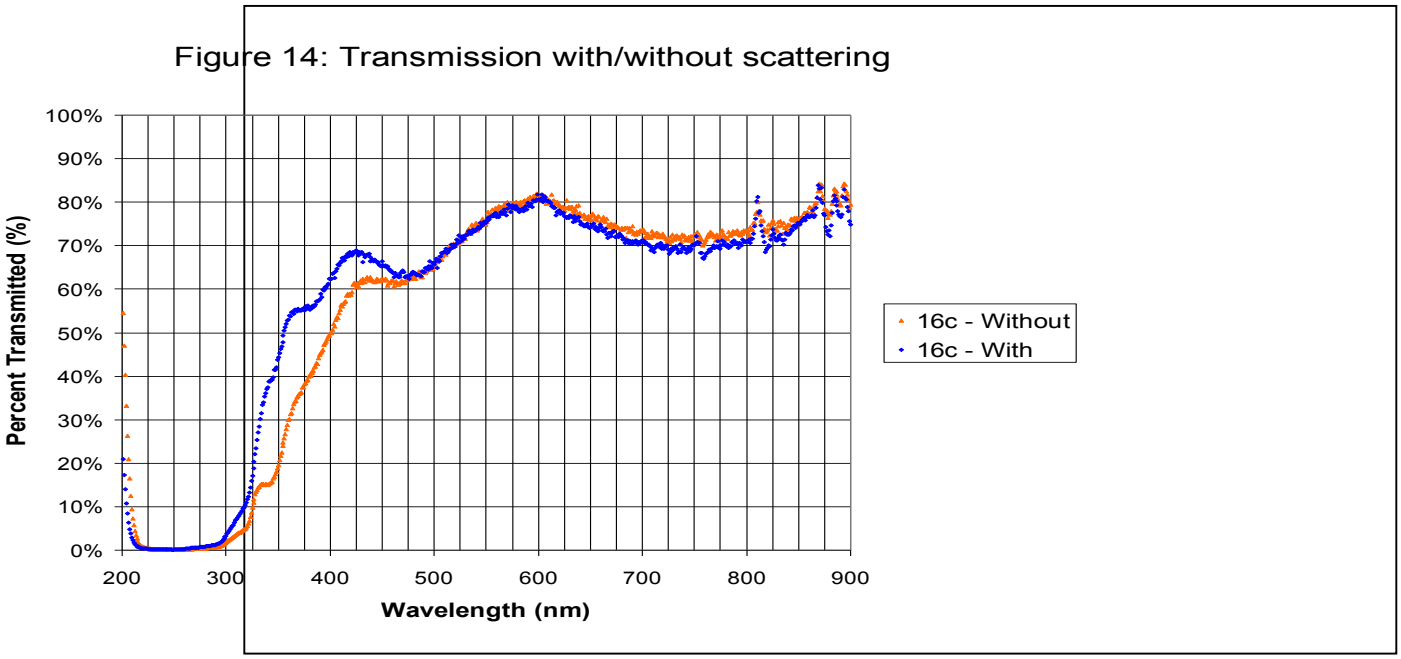

shows the results of these measurements. The two spectra overlap fairly well through most of the spectrum but below about 450 nm they differ significantly. Since this region of scattering influence occurs within the transition from weak absorption to strong absorption, its relevance with respect to the determination of the absorption coefficient, the Egap, and the type of gap transition should be evident. A further significance of the fact that more scattering appears in the blue end of the visible spectrum than the red, leads one to suspect Rayleigh scattering, the same mechanism that colors the sky blue due to the same sort of nonuniform scattering.

To investigate this further, measurement of scattered light spectra can be made using the integrating sphere described in Appendix B. Figure 15 shows the resulting scattered transmission and reflection spectra. A theoretical curve representing the $(1/\lambda^4)$ dependence of Rayleigh scattering has also been included for comparison. The general agreement in spectral behavior between the transmission curve and the Rayleigh theory curve suggests that Rayleigh scattering is indeed occurring. Rayleigh scattering occurs

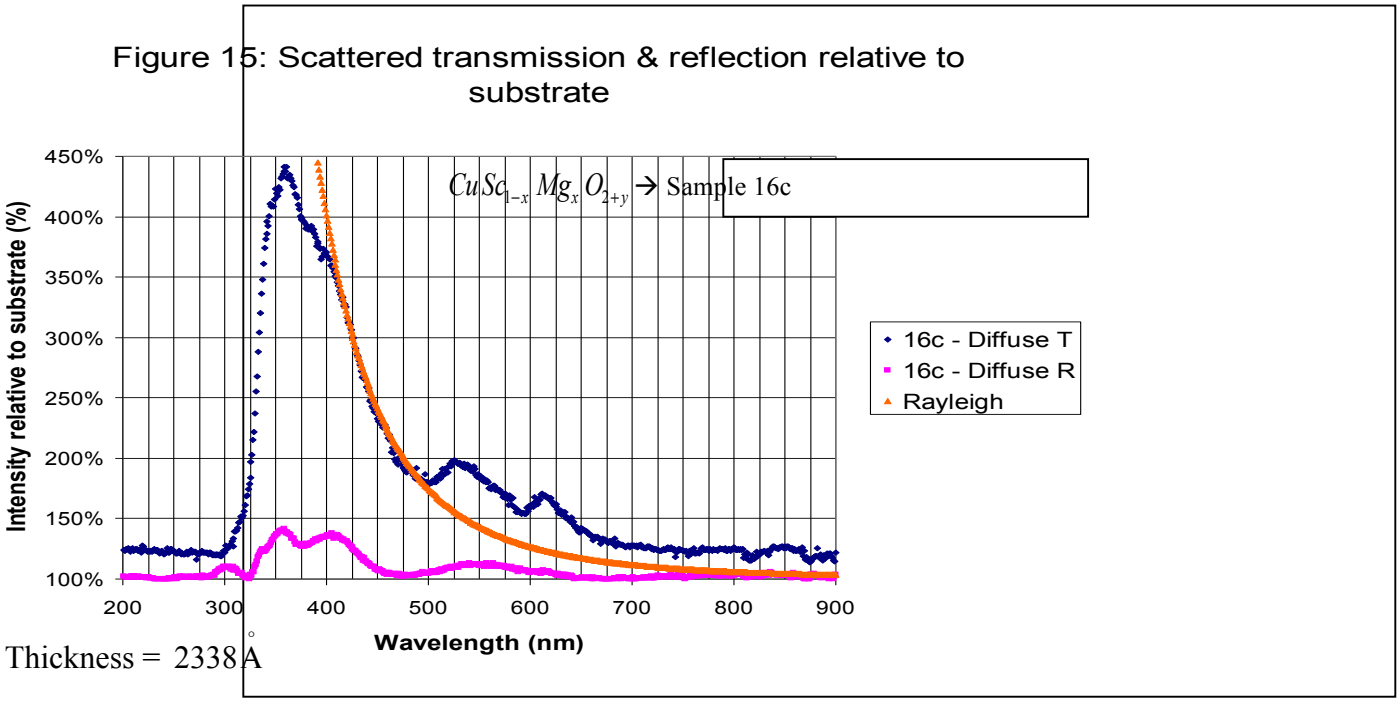

Thickness = 2338 Å

when incident light encounters particles that are smaller than about $(\lambda/15)$. One can deduce then that the scattering particles are approximately 10-20 nm across. Since this is too large to be associated with atomic impurities, one might conclude that the grain boundaries are therefore responsible for the scattering. Further investigation with an atomic force microscope (AFM) verifies that the grain size does in fact fit into this range. The reflection curve, while showing a similar bias towards scattering at lower wavelengths, doesn't show a distinct likeness to the Rayleigh curve. What is clear is that the diffuse transmission and reflection spectra both have relevant spectral structure that can influence the directly measured spectra.

Conclusion

The basics of transparent conductor research have been discussed. In general, transparent conductors are designed from wide Egap materials that have been "doped" with impurities that allow conduction at room temperature. Methods have been shown for the calculation of the optical constants related to any transparent conductive thin film material system deposited in a single layer on transparent substrate. Using the measured film thickness, the wavelength dependent refractive index $n(\lambda)$ was determined from the minima and maxima of the thin film interference fringes present in both the transmittance and reflectance spectra.

Both complex and simple methods for calculating the wavelength dependent absorption coefficient $\alpha(\lambda)$ have been described. In the simple model, the relation $\left(T/1-R\right)$ was used to achieve a "fringe free" curve that is proportional to absorption. In the complex model, the rigorous derivation of reflectance and transmittance from the Fresnel amplitude coefficients was used to determine a scale factor that corrects for the infinite internal reflections from the back surface of the film. This correction results in a more accurate absorption coefficient spectrum. It has been show that both the simple and complex derivation of $\alpha(\lambda)$ will result in the same calculated Egap. A method of investigating the direct or indirect nature of the energy gap transition by attempting to linearize the plot of the absorption coefficient has also been shown.

Diffuse transmittance and reflectance spectra were measured using an integrating sphere and compared to "close-up" and "far-away" measurements of direct transmittance and reflectance. These comparisons demonstrated the presence of spectral structure due to Rayleigh scattering.

Overall, a reasonably simple approach, using only readily measurable quantities, for determining the optical constants for a thin film sample has been demonstrated.

BIBLIOGRAPHY

Driscoll, W.G., editor. 1978. *Handbook of Optics.* New York: McGraw Hill.

Hecht, E. 1998. *Optics*. 3rd ed. Massachusetts: Addison-Wesley.

Hishikawa, Y., et al. 1991. Interference-Free Determination of the Optical Absorption Coefficient and the Optical Gap of Amorphous Silicon Thin Films. *Japanese Journal of Applied Physics*. Vol. 30, No. 5, May 1991, pp. 1008-1014.

Pankove, J.I. 1971. *Optical Processes in Semiconductors.* New York: Dover Publications, Inc.

Peyghambarian, N., S.W. Koch, and A. Mysyrowicz. 1993. *Introduction to Semiconductor Optics.* New Jersey: Prentice Hall.

Pierret, R.F. 1996. *Semiconductor Device Fundamentals.* Massachusetts: Addison-Wesley Publishing Company.

Schroder, D.K. 1998. *Semiconductor Material and Device Characterization.* 2nd ed. New York: John Wiley & Sons, Inc.

Swanepoel, R. 1983. Determination of the thickness and optical constants of amorphous silicon. *Journal of Physics E.* Vol. 16, 1983, pp. 1214-1222

Appendix A: How does the color of visible light relate to energy?

To understand the relationship between photon energy and color, one must begin with the total relativistic energy of a particle, $E = \sqrt{(pc)^2 + (mc^2)^2}$. However, the rest energy ($E_0 = mc^2$) of a photon is zero. Thus, the total energy of a photon is ($E = pc$), where (p) represents the momentum of the photon and (c) represents the speed of light in a vacuum. Recalling De Broglie's relation, the wavelength of any particle moving with momentum (p) can be defined as ($\lambda = h/p$), where ($h = 4.136 \times 10^{-15}\, eV \cdot s$) is Planck's constant. By substituting this relation into the equation for photon energy, a useful relation between the wavelength of a photon and its energy emerges:

Violet ~ 400nm
Blue ~ 475nm
Green ~ 525nm
Yellow ~ 575nm
Orange ~ 600nm
Red ~ 675nm

$$PhotonEnergy = E = \frac{hc}{\lambda} = \frac{1240 eV \cdot nm}{Wavelength(nm)}$$

- Using the above relation, one can tabulate the approximate energies of the various colors of the visible spectrum as shown below:

Color	Wavelength (nm)	Energy (eV)
Violet	400.00	3.10
Blue	475.00	2.61
Green	525.00	2.36
Yellow	575.00	2.16
Orange	600.00	2.07
Red	675.00	1.84

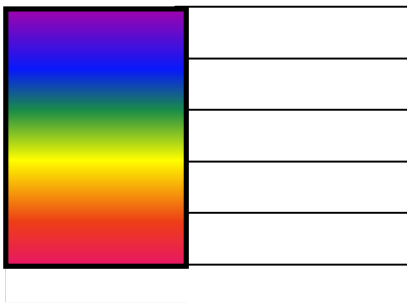

Appendix B: General Experimental Setup

-Source Section of System-

- Power Supply (Not shown):
  - Schoeffel LPS251 Lamp Power Supply (for Xe Lamp)
  - Kepco ATE 36-8M Power Supply (for QTH Lamp)

- Light Source: Oriel model 7340 Universal Monochromator Illuminator
  - Option 1: 150W Xenon lamp
  - Option 2: 100W Quartz Tungsten Halogen lamp (Operated at 6A*10V=60W)

- Double Monochromator: Oriel model 77276
  - Consists of two Oriel model 77250 monochromators in series
  - Coupled stepper motor drive for synchronized scanning
  - Input, output, and center slits are interchangeable
  - Identical interchangeable reflection gratings

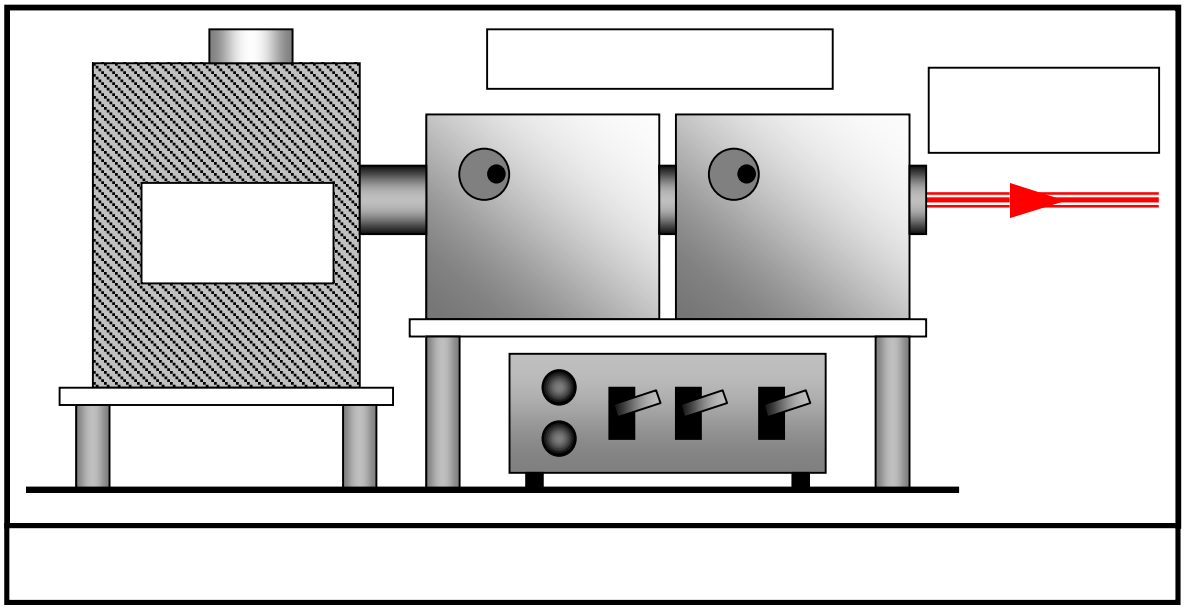

Figure B-1: Monochromatic source section of spectrometer system

-Oriel model 7340 Universal Monochromator Illuminator-

The Oriel 7340 holds two lamps whose outputs can be isolated by turning a shutter knob. The lamps used in this system are the quartz tungsten halogen (QTH) and xenon (Xe) arc lamps listed on the previous page. The QTH lamp is rated at 100-watts but is typically operated at 60-watts, while the Xe lamp is operated at the specified 150-watts. The illuminator is arranged such that the chosen lamp is imaged directly on the entrance slit of the first monochromator. To maximize monochromator throughput, a 3.16-mm entrance slit (20-nm bandpass) was used in conjunction with 1.56-mm center and exit slits (10-nm bandpass) achieving a theoretical 5-nm-output resolution.

-Oriel model 77276 Double Monochromator-

The Oriel 77276 holds an identical reflection grating in each Oriel model 77250 housing. The 250nm grating is blazed, or optimized, for 250nm light. The 500nm grating is similarly blazed such that the reflected intensity is optimized at incident wavelengths of 500nm. Figure B-2 shows a spectral comparison of the lamp sources using two different sets of gratings. This data shows that using the xenon lamp with 250nm gratings will provide the best results in the ultraviolet region of the spectrum.

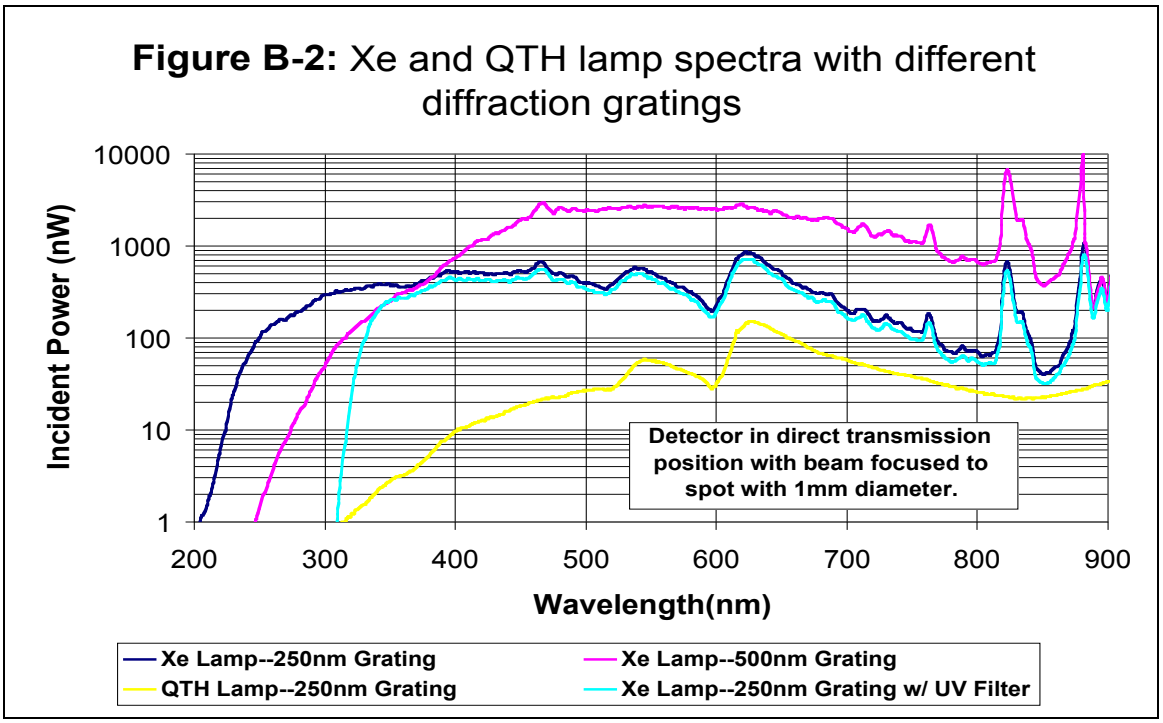

Figure B-2: Xe and QTH lamp spectra with different diffraction gratings

-Measurement Section of System-

- Mirrors: Newport 10D10AL.2
  - Flat pyrex mirror, 25.4mm diameter, 1/5 wave
  - R>90% avg., 250-600nm

- Lenses: Plano-convex lens, UV grade fused silica, 25.4mm diameter
  - Newport SPX028- 200mm focal length
  - Newport SPX022- 100mm focal length

- Power Meter: Newport model 835 Optical Power Meter
  - Pico-watt sensitivity, GPIB interface
  - UV sensitive photodetector

- Integrating Sphere: Oriel model 70491 Integrating Sphere
  - 4-ports, reflectance/transmittance measurement capability
  - 8-inch interior diameter
  - Barium sulfate ($BaSO_4$) based, white interior coating (R>95%)

- Sample Holders:
  - Direct measurements (no sphere)
    - Spring-clip on optical post with degree of incidence measure
  - Sphere measurements
    - Custom two-axis rotation mount on optical post
    - Standard lens mount on optical post (holds cup for powder measurements)

- Light-tight Box:
  - The entire measurement section of the system is enclosed within a homemade light-tight cardboard box wrapped in black plastic and aluminum foil. This effectively negates the noise introduced by intruding room lights

Input
Sample
Input
Port Plug
Reflection

-Direct Reflection and Transmission-

To measure the direct reflection and transmission of the incident beam for a given sample, it is most convenient to use the configuration depicted in Figure B-3. Here the input beam is directed from the output of the monochromator to the sample with a series of two mirrors. This beam is then focused with the 100mm focal length lens such that a minimal spot is incident on the sample and also the face of the detector. The sample is held in a mount with an angle measure so that the deviation from normal incidence can be measured for use in later calculations.

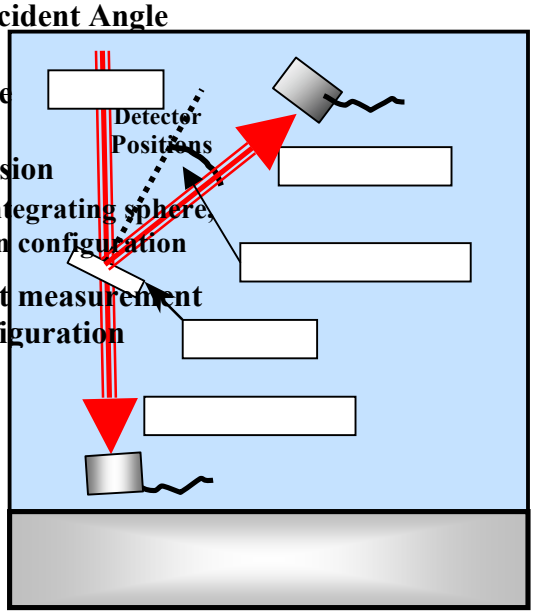

Figure B-4: Integrating sphere, transmission configuration

Input
Detector Positions
Sample

Figure B-3: Direct measurement sample configuration

Figure B-5: Integrating sphere, reflection configuration

-Diffuse Reflection and Transmission-

To measure diffuse reflection and transmission, an integrating sphere can be employed. An integrating sphere acts as an ideal optical diffuser which provides a spatially independent illumination incident on the interior surface of the sphere. This allows the measurement the diffuse intensity from the side port location in a entirely uniform manner. The integrating sphere is designed to make both diffuse and direct measurements, but in practice it is more convenient to use the sphere only for the diffuse measurements because of the potential for damaging the highly reflective interior coating. In this system, the monochromator output can be directed to the integrating sphere or the arrangement in Figure B-3 by means of two interchangeable mirrors on kinematic mounts.

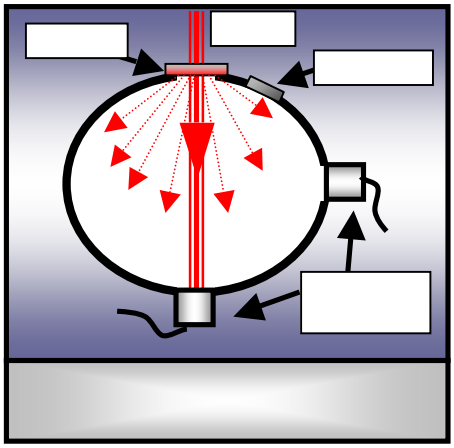

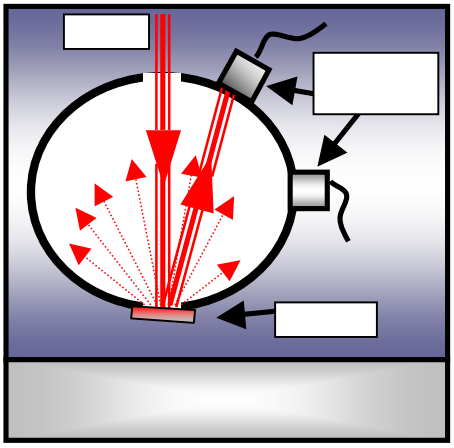

-Integrating Sphere Calibration-

When using the integrating sphere as part of the spectrometer system, its unknown spectral response must be taken into consideration. The spectral response of the sphere can be calibrated using known calibration port plugs mounted in the bottom port of the sphere. Two such calibration standards were used to calibrate this system. One has a uniform, wavelength independent 50% reflectance. The other has strong erbium absorption lines at known wavelengths. This data is shown normalized to the spectral response of the sphere's internal coating in Figure B-6 below.

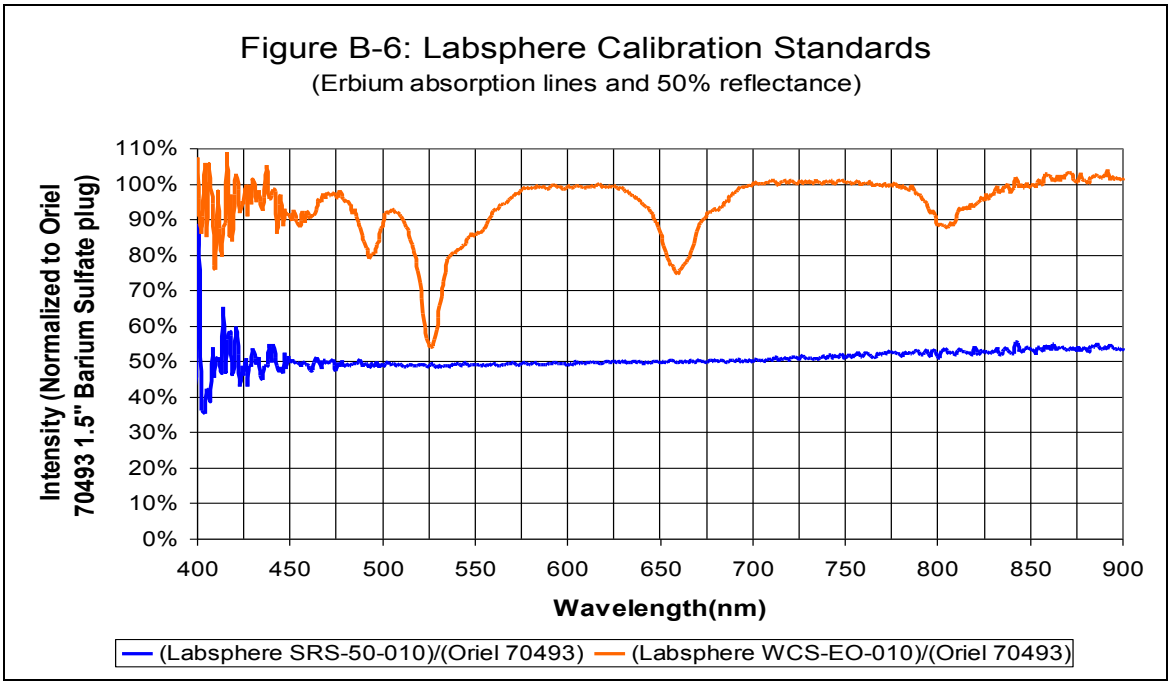

The calibration data shown above verifies the uniform response of the integrating sphere. The erbium lines match the known standard, the 50% standard is primarily uniform across the measured spectrum, and no anomalous spectral structure is apparent. It should be noted that this calibration was carried out using the quartz tungsten halogen lamp. This lamp's inherent lack of intensity in the ultraviolet region of the spectrum introduces noise into the data as the signal strength becomes very low.

Appendix C: Determining the Index of Refraction

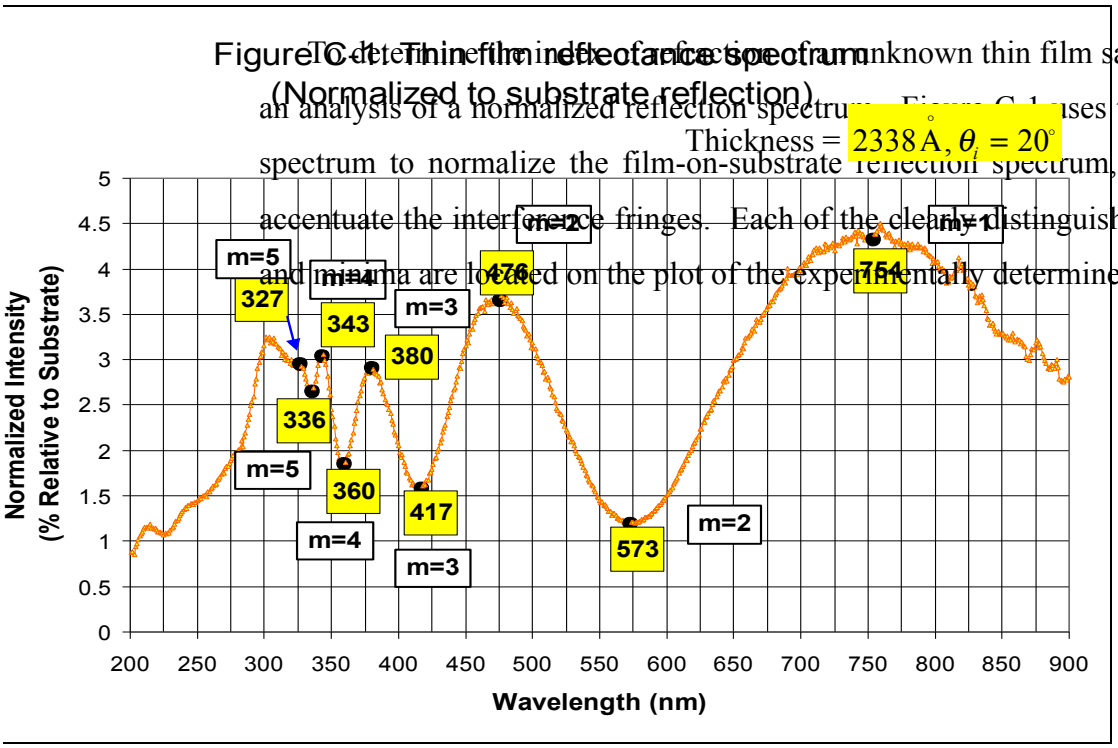

Figure C-1: Thin film reflectance spectrum

To determine the index of refraction of an unknown thin film sample, one begins with an analysis of a normalized reflection spectrum. Figure C-1 uses the substrate reflection spectrum to normalize the film-on-substrate reflection spectrum, which serves only to accentuate the interference fringes. Each of the clearly distinguishable intensity maxima and minima are located on the plot of the experimentally determined spectrum.

These marked wavelengths will correspond to values tabulated from equations (19), for both λ_{MAX} and λ_{MIN}. In Table C-1 and Table C-2 on the following pages, one finds that the zeroth order fringe correlates to none of the marked data points. This, while not an absolute determination, indicates that the lowest order fringe visible in the measured data is the (m=1) maxima fringe and the (m=2) minima fringe. One then simply scans down the (m=1) or (m=2) column in the appropriate table to find the predetermined wavelength and then match it to the refractive index listed in that row, then similarly for additional higher order fringes. Table C-3 shows the results of this process.

Table C-1: Wavelengths of Reflection Maxima for Different Refractive Indices								
**Match the wavelength and fringe order				Sample Thickness(d) in (nm)				233.8
from collected data to table below				Incident Angle(in Radians)				0.349
Fringe#(m)	0	1	2	3	4	5	6	7
Index(n)	Wavelength in (nm) of the associated reflection maxima							
1.5	1365.9	455.3	273.2	195.1	151.8	124.2	105.1	91.1
1.55	1413.8	471.3	282.8	202.0	157.1	128.5	108.8	94.3
1.6	1461.7	487.2	292.3	208.8	162.4	132.9	112.4	97.4
1.65	1509.6	503.2	301.9	215.7	167.7	137.2	116.1	100.6
1.7	1557.3	519.1	311.5	222.5	173.0	141.6	119.8	103.8
1.75	1605.1	535.0	321.0	229.3	178.3	145.9	123.5	107.0
1.8	1652.7	550.9	330.5	236.1	183.6	150.2	127.1	110.2
1.85	1700.3	566.8	340.1	242.9	188.9	154.6	130.8	113.4
1.9	1747.9	582.6	349.6	249.7	194.2	158.9	134.5	116.5
1.95	1795.4	598.5	359.1	256.5	199.5	163.2	138.1	119.7
2	1842.9	614.3	368.6	263.3	204.8	167.5	141.8	122.9
2.05	1890.3	630.1	378.1	270.0	210.0	171.8	145.4	126.0
2.1	1937.7	645.9	387.5	276.8	215.3	176.2	149.1	129.2
2.15	1985.1	661.7	397.0	283.6	220.6	180.5	152.7	132.3
2.2	2032.4	677.5	406.5	290.3	225.8	184.8	156.3	135.5
2.25	2079.8	693.3	416.0	297.1	231.1	189.1	160.0	138.7
2.3	2127.1	709.0	425.4	303.9	236.3	193.4	163.6	141.8
2.35	2174.3	724.8	434.9	310.6	241.6	197.7	167.3	145.0
2.4	2221.6	740.5	444.3	317.4	246.8	202.0	170.9	148.1
2.45	2268.8	756.3	453.8	324.1	252.1	206.3	174.5	151.3
2.5	2316.0	772.0	463.2	330.9	257.3	210.5	178.2	154.4
2.55	2363.2	787.7	472.6	337.6	262.6	214.8	181.8	157.5
2.6	2410.4	803.5	482.1	344.3	267.8	219.1	185.4	160.7
2.65	2457.6	819.2	491.5	351.1	273.1	223.4	189.0	163.8
2.7	2504.7	834.9	500.9	357.8	278.3	227.7	192.7	167.0
2.75	2551.8	850.6	510.4	364.5	283.5	232.0	196.3	170.1
2.8	2599.0	866.3	519.8	371.3	288.8	236.3	199.9	173.3
2.85	2646.1	882.0	529.2	378.0	294.0	240.6	203.5	176.4
2.9	2693.2	897.7	538.6	384.7	299.2	244.8	207.2	179.5
2.95	2740.2	913.4	548.0	391.5	304.5	249.1	210.8	182.7
3	2787.3	929.1	557.5	398.2	309.7	253.4	214.4	185.8
3.05	2834.4	944.8	566.9	404.9	314.9	257.7	218.0	189.0
3.1	2881.4	960.5	576.3	411.6	320.2	261.9	221.6	192.1
3.15	2928.5	976.2	585.7	418.4	325.4	266.2	225.3	195.2
3.2	2975.5	991.8	595.1	425.1	330.6	270.5	228.9	198.4
3.25	3022.5	1007.5	604.5	431.8	335.8	274.8	232.5	201.5
3.3	3069.5	1023.2	613.9	438.5	341.1	279.0	236.1	204.6
3.35	3116.6	1038.9	623.3	445.2	346.3	283.3	239.7	207.8
3.4	3163.6	1054.5	632.7	451.9	351.5	287.6	243.4	210.9
3.45	3210.6	1070.2	642.1	458.7	356.7	291.9	247.0	214.0
3.5	3257.5	1085.8	651.5	465.4	361.9	296.1	250.6	217.2
3.55	3304.5	1101.5	660.9	472.1	367.2	300.4	254.2	220.3
3.6	3351.5	1117.2	670.3	478.8	372.4	304.7	257.8	223.4
3.65	3398.5	1132.8	679.7	485.5	377.6	309.0	261.4	226.6
3.7	3445.4	1148.5	689.1	492.2	382.8	313.2	265.0	229.7
3.75	3492.4	1164.1	698.5	498.9	388.0	317.5	268.6	232.8
3.8	3539.3	1179.8	707.9	505.6	393.3	321.8	272.3	236.0
3.85	3586.3	1195.4	717.3	512.3	398.5	326.0	275.9	239.1
3.9	3633.2	1211.1	726.6	519.0	403.7	330.3	279.5	242.2
3.95	3680.2	1226.7	736.0	525.7	408.9	334.6	283.1	245.3
4	3727.1	1242.4	745.4	532.4	414.1	338.8	286.7	248.5

Table C-2: Wavelengths of Reflection Minima for Different Refractive Indices								
**Match the wavelength and fringe order				Sample Thickness(d) in (nm)				233.8
from collected data to table below				Incident Angle(in Radians)				0.349
Fringe#(m)	0	1	2	3	4	5	6	7
Index(n)	Wavelength in (nm) of the associated reflection minima							
1.5	#DIV/0!	682.9	341.5	227.6	170.7	136.6	113.8	97.6
1.55	#DIV/0!	706.9	353.5	235.6	176.7	141.4	117.8	101.0
1.6	#DIV/0!	730.9	365.4	243.6	182.7	146.2	121.8	104.4
1.65	#DIV/0!	754.8	377.4	251.6	188.7	151.0	125.8	107.8
1.7	#DIV/0!	778.7	389.3	259.6	194.7	155.7	129.8	111.2
1.75	#DIV/0!	802.5	401.3	267.5	200.6	160.5	133.8	114.6
1.8	#DIV/0!	826.4	413.2	275.5	206.6	165.3	137.7	118.1
1.85	#DIV/0!	850.2	425.1	283.4	212.5	170.0	141.7	121.5
1.9	#DIV/0!	873.9	437.0	291.3	218.5	174.8	145.7	124.8
1.95	#DIV/0!	897.7	448.8	299.2	224.4	179.5	149.6	128.2
2	#DIV/0!	921.4	460.7	307.1	230.4	184.3	153.6	131.6
2.05	#DIV/0!	945.1	472.6	315.0	236.3	189.0	157.5	135.0
2.1	#DIV/0!	968.9	484.4	323.0	242.2	193.8	161.5	138.4
2.15	#DIV/0!	992.5	496.3	330.8	248.1	198.5	165.4	141.8
2.2	#DIV/0!	1016.2	508.1	338.7	254.1	203.2	169.4	145.2
2.25	#DIV/0!	1039.9	519.9	346.6	260.0	208.0	173.3	148.6
2.3	#DIV/0!	1063.5	531.8	354.5	265.9	212.7	177.3	151.9
2.35	#DIV/0!	1087.2	543.6	362.4	271.8	217.4	181.2	155.3
2.4	#DIV/0!	1110.8	555.4	370.3	277.7	222.2	185.1	158.7
2.45	#DIV/0!	1134.4	567.2	378.1	283.6	226.9	189.1	162.1
2.5	#DIV/0!	1158.0	579.0	386.0	289.5	231.6	193.0	165.4
2.55	#DIV/0!	1181.6	590.8	393.9	295.4	236.3	196.9	168.8
2.6	#DIV/0!	1205.2	602.6	401.7	301.3	241.0	200.9	172.2
2.65	#DIV/0!	1228.8	614.4	409.6	307.2	245.8	204.8	175.5
2.7	#DIV/0!	1252.4	626.2	417.5	313.1	250.5	208.7	178.9
2.75	#DIV/0!	1275.9	638.0	425.3	319.0	255.2	212.7	182.3
2.8	#DIV/0!	1299.5	649.7	433.2	324.9	259.9	216.6	185.6
2.85	#DIV/0!	1323.0	661.5	441.0	330.8	264.6	220.5	189.0
2.9	#DIV/0!	1346.6	673.3	448.9	336.6	269.3	224.4	192.4
2.95	#DIV/0!	1370.1	685.1	456.7	342.5	274.0	228.4	195.7
3	#DIV/0!	1393.7	696.8	464.6	348.4	278.7	232.3	199.1
3.05	#DIV/0!	1417.2	708.6	472.4	354.3	283.4	236.2	202.5
3.1	#DIV/0!	1440.7	720.4	480.2	360.2	288.1	240.1	205.8
3.15	#DIV/0!	1464.2	732.1	488.1	366.1	292.8	244.0	209.2
3.2	#DIV/0!	1487.8	743.9	495.9	371.9	297.6	248.0	212.5
3.25	#DIV/0!	1511.3	755.6	503.8	377.8	302.3	251.9	215.9
3.3	#DIV/0!	1534.8	767.4	511.6	383.7	307.0	255.8	219.3
3.35	#DIV/0!	1558.3	779.1	519.4	389.6	311.7	259.7	222.6
3.4	#DIV/0!	1581.8	790.9	527.3	395.4	316.4	263.6	226.0
3.45	#DIV/0!	1605.3	802.6	535.1	401.3	321.1	267.5	229.3
3.5	#DIV/0!	1628.8	814.4	542.9	407.2	325.8	271.5	232.7
3.55	#DIV/0!	1652.3	826.1	550.8	413.1	330.5	275.4	236.0
3.6	#DIV/0!	1675.7	837.9	558.6	418.9	335.1	279.3	239.4
3.65	#DIV/0!	1699.2	849.6	566.4	424.8	339.8	283.2	242.7
3.7	#DIV/0!	1722.7	861.4	574.2	430.7	344.5	287.1	246.1
3.75	#DIV/0!	1746.2	873.1	582.1	436.5	349.2	291.0	249.5
3.8	#DIV/0!	1769.7	884.8	589.9	442.4	353.9	294.9	252.8
3.85	#DIV/0!	1793.1	896.6	597.7	448.3	358.6	298.9	256.2
3.9	#DIV/0!	1816.6	908.3	605.5	454.2	363.3	302.8	259.5
3.95	#DIV/0!	1840.1	920.0	613.4	460.0	368.0	306.7	262.9
4	#DIV/0!	1863.6	931.8	621.2	465.9	372.7	310.6	266.2

Figure C-2: Least squares fit to data using Maple 6 software

```
> restart:with(plots):
Warning, the name changecoords has been redefined
> with(stats):
Least squares fit to Cauchy's formula for the wavelength dependent refractive index:
> fit[leastsquare[[x,n], n=a/x^6+b/x^4+c/x^2+d]]([327,336,343,360,380,417,476,573,754],[3.86,3.61,3.52,3.1,2.87,
2.7,2.57,2.48,2.44]);
```

$$n = .5759846518\,10^{16}\frac{1}{x^6} - \frac{.6216914423\,10^{11}}{x^4} + \frac{261590.1778}{x^2} + 2.127563248$$

```
> n:=.5759846518e16*1/(x^6)-
6216914423e11/(x^4)+261590.1778/(x^2)+2.127563248:
> plot(n,x=300..900,view=[300..900,2..4]);
```

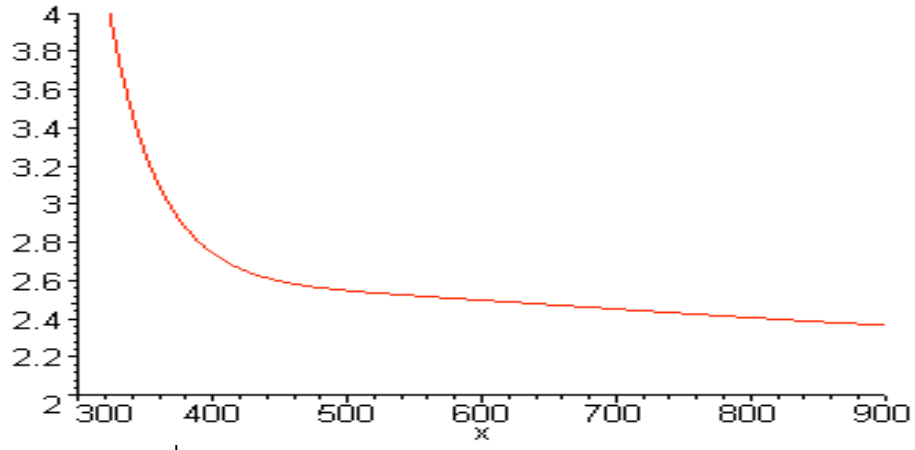

Table C-3: Refractive Index

Wavelength (nm)	Index (n)
327	3.86
336	3.61
343	3.52
360	3.1
380	2.87
417	2.7
476	2.57
573	2.48
754	2.44

There are now nine data points, listed in Table C-3, that give a good indication of the magnitude and behavior of the wavelength dependent refractive index of the thin film sample. It is now a simple matter to derive a continuous functional representation of the refractive index using any mathematics software. The Maple code for doing so is depicted in Figure C-2 where the data points in Table

nto a spreadsheet program and

e spectra.

How does the color of visible light relate to energy?

There is a simple and fundamental relationship between the color of light and the energy of the associated photons that humans perceive as colored light.

- The visible portion of the electromagnetic spectrum is shown below:

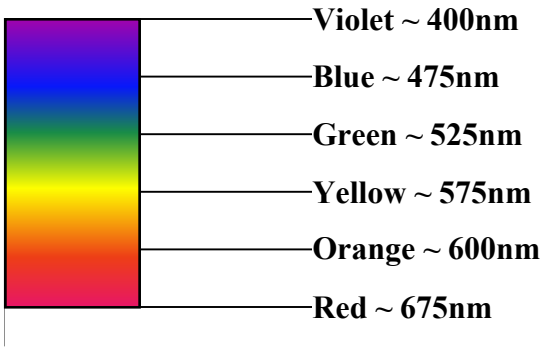

- The wavelengths of different colors can be easily converted to energy via the relation shown below:

$$PhotonEnergy = E = \frac{hc}{\lambda} = \frac{1240eV \cdot nm}{Wavelength(nm)}$$

- Using the above relation, one can tabulate the approximate energies of the various colors of the visible spectrum as shown below:

Color	Wavelength (nm)	Energy (eV)
Violet	400.00	3.10
Blue	475.00	2.61
Green	525.00	2.36
Yellow	575.00	2.16
Orange	600.00	2.07
Red	675.00	1.84

General Experimental Setup

-Source Section of System-

- Power Supply (Not shown):
  - Schoeffel LPS251 Lamp Power Supply (for Xe Lamp)
  - Kepco (Insert MODEL#) (for QTH Lamp)

- Light Source: Oriel model 7340 Universal Monochromator Illuminator
  - Option 1: !50W Xenon arc lamp
  - Option 2: 100W Quartz Tungsten Halogen lamp

- Double Monochromator: Oriel model 77276
  - Consists of two Oriel model 77250 monochromators in series
  - Coupled stepper motor drive for synchronized scanning
  - Input, output, and center slits are interchangeable
  - Identical interchangeable reflection gratings

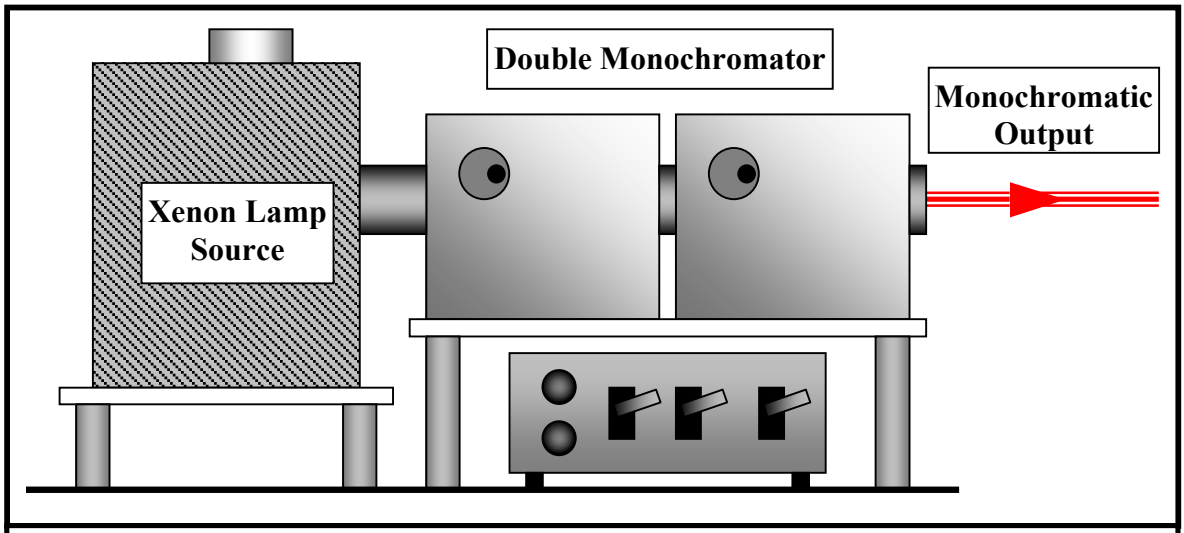

Figure B-1: Monochromatic Source Section of Spectrometer System

-Oriel model 7340 Universal Monochromator Illuminator-

The Oriel 7340 holds two lamps whose outputs can be isolated by turning a shutter knob. The lamps used in this system are the quartz tungsten halogen (QTH) and xenon (Xe) arc lamps listed on the previous page. The QTH lamp is rated at 100-watts but is typically operated at 60-watts, while the Xe lamp is operated at the specified 150-watts. The illuminator is arranged such that the chosen lamp is imaged directly on the entrance slit of the first monochromator. To maximize monochromator throughput, a 3.16mm entrance slit (20nm bandpass) was used in conjunction with 1.56mm center and exit slits (10nm bandpass) achieving a theoretical 5nm-output resolution.

-Oriel model 77276 Double Monochromator-

The Oriel 77276 holds an identical reflection grating in each Oriel model 77250 housing. The 250nm grating is blazed, or optimized, for 250nm light. The 500nm grating is similarly blazed such that the reflected intensity is optimized at incident wavelengths of 500nm. Figure B-2 shows a spectral comparison of the lamp sources using two different sets of gratings. This data shows that using the xenon lamp with 250nm gratings will provide the best results in the ultraviolet region of the spectrum.

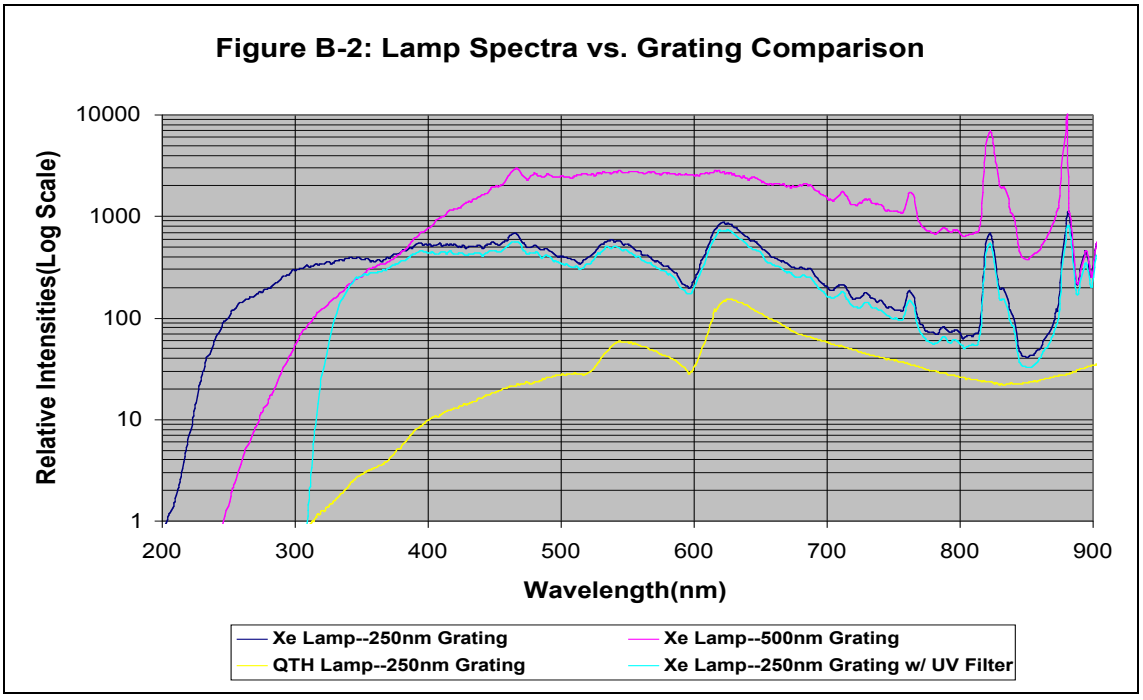

-Measurement Section of System-

- Mirrors: Newport 10D10AL.2
  - Flat pyrex mirror, 25.4mm diameter, 1/5 wave
  - R>90% avg., 250-600nm

- Lenses: Plano-convex lens, UV grade fused silica, 25.4mm diameter
  - Newport SPX028- 200mm focal length
  - Newport SPX022- 100mm focal length

- Power Meter: Newport model 835 Optical Power Meter
  - Pico-watt sensitivity, GPIB interface
  - UV sensitive photodetector

- Integrating Sphere: Oriel model 70491 Integrating Sphere
  - 4-ports, reflectance/transmittance measurement capability
  - 8-inch interior diameter
  - Barium sulfate ($BaSO_4$) based, white interior coating (R>95%)

- Sample Holders:
  - Direct measurements (no sphere)
    - Spring-clip on optical post with degree of incidence measure
  - Sphere measurements
    - Custom two-axis rotation mount on optical post
    - Standard lens mount on optical post (holds cup for powder measurements)

- Light-tight Box:
  - The entire measurement section of the system is enclosed within a homemade light-tight cardboard box wrapped in black plastic and aluminum foil. This effectively negates the noise introduced by intruding room lights

-Direct Reflection and Transmission-

To measure the direct reflection and transmission of the incident beam for a given sample, it is most convenient to use the configuration depicted in Figure B-3. Here the input beam is directed from the output of the monochromator to the sample with a series of two mirrors. This beam is then focused with the 100mm focal length lens such that a minimal spot is incident on the sample and also the face of the detector. The sample is held in a mount with an angle measure so that the deviation from normal incidence can be measured for use in later calculations.

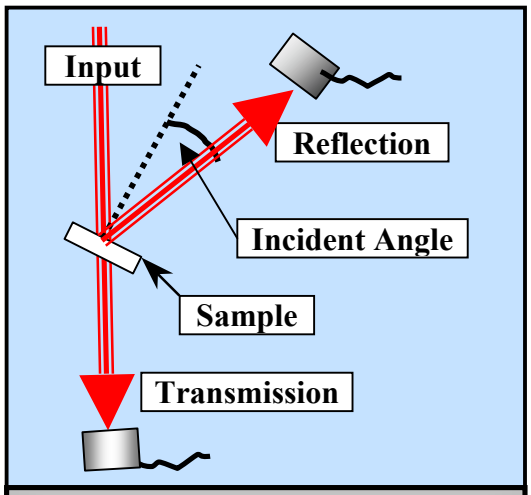

Figure B-3: Direct Measurement Sample Configuration

-Scattered Reflection and Transmission-

To measure scattered reflection and transmission, an integrating sphere can be employed. An integrating sphere acts as an ideal optical diffuser which provides a spatially independent illumination incident on the interior surface of the sphere. This allows the measurement the scattered intensity from the side port location in a entirely uniform manner. The integrating sphere is designed to make both scattered and direct measurements, but in practice it is more convenient to use the sphere only for the scattered measurements because of the potential for damaging the highly reflective interior coating. In this system, the monochromator output can be directed to the integrating sphere or the arrangement in Figure B-3 by means of two interchangeable mirrors on kinematic mounts.

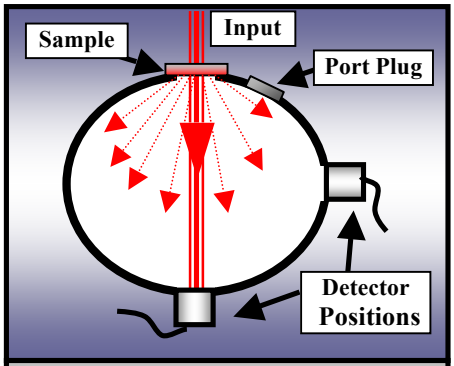

Figure B-4: Integrating sphere, transmission configuration

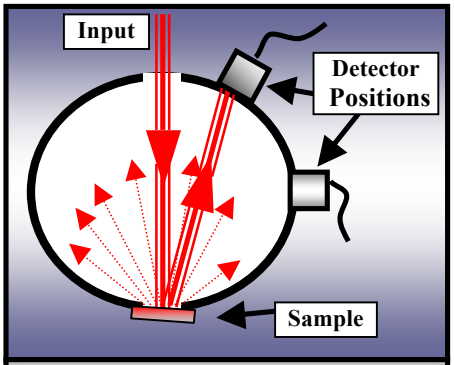

Figure B-5: Integrating sphere, reflection configuration

-Integrating Sphere Calibration-

When using the integrating sphere as part of the spectrometer system, its unknown spectral response must be taken into consideration. The spectral response of the sphere can be calibrated using known calibration port plugs mounted in the bottom port of the sphere. Two such calibration standards were used to calibrate this system. One has a uniform, wavelength independent 50% reflectance. The other has strong erbium absorption lines at known wavelengths. This data is shown normalized to the spectral response of the sphere's internal coating in Figure B-6 below.

Figure B-6: Labsphere Calibration Standards
(Erbium absorption lines and 50% reflectance)

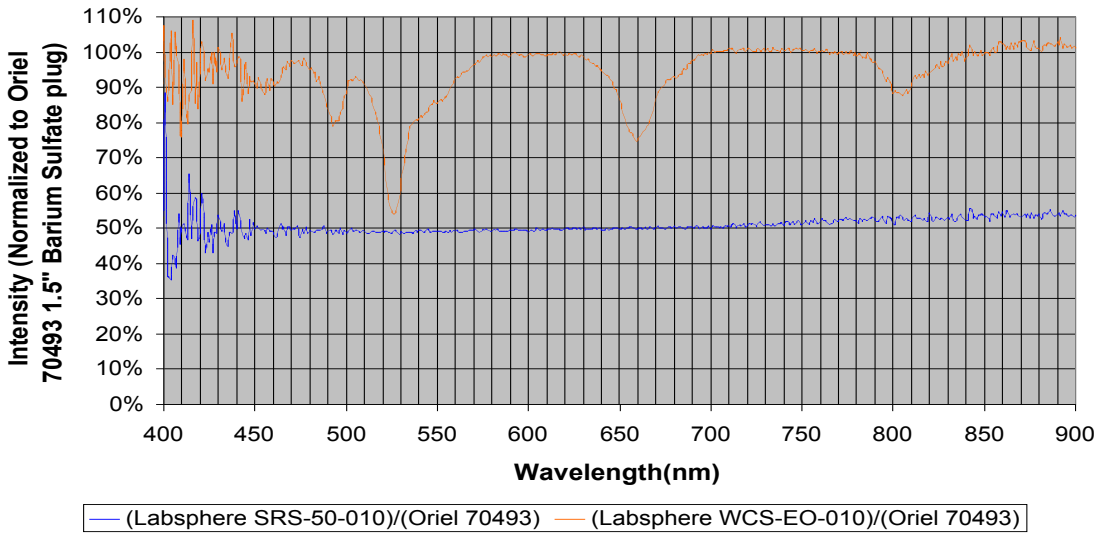

The calibration data shown above verifies the uniform response of the integrating sphere. The erbium lines match the known standard, the 50% standard is primarily uniform across the measured spectrum, and no anomalous spectral structure is apparent. It should be noted that this calibration was carried out using the quartz tungsten halogen lamp. This lamp's inherent lack of intensity in the ultraviolet region of the spectrum introduces noise into the data as the signal strength becomes very low.

Determining the Index of Refraction

To determine the index of refraction of an unknown thin film sample, one begins with an analysis of a normalized reflection spectrum. Figure C-1 uses the substrate reflection spectrum to normalize the film-on-substrate reflection spectrum, which serves only to accentuate the interference fringes. Each of the clearly distinguishable intensity maxima and minima are located on the plot of the experimentally determined spectrum.

Figure C-1: Thin Film Reflectance Spectrum
(20 degree incidence--Normalized to Substrate Reflection)
(Sample SM16C - Thickness 233.8nm)

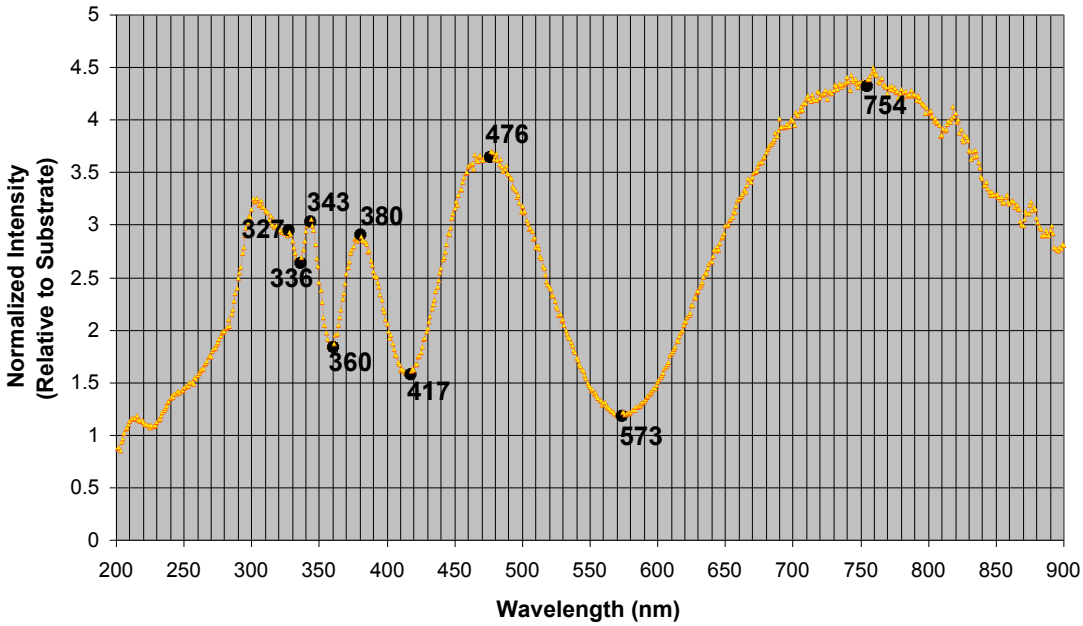

These marked wavelengths will correspond to tabulated values derived from the equations for both λ_{MAX} and λ_{MIN} in Figure 7. In Table C-1 and Table C-2 on the following pages, one finds that the zeroth order fringe correlates to none of the marked data points. This, while not an absolute determination, indicates that the lowest order fringe visible in the measured data is the (m=1) fringe. One then simply scans down the (m=1) column to find the appropriate wavelength and then match it to the refractive index listed in that row, then similarly for additional higher order fringes. Table C-3 shows the results of this process.

Table C-1: Wavelengths of Reflection Maxima for Different Refractive Indices								
**Match the wavelength and fringe order				Sample Thickness(d) in (nm)				233.8
from collected data to table below				Incident Angle(in Radians)				0.349
Fringe#(m)	0	1	2	3	4	5	6	7
Index(n)	Wavelength in (nm) of the associated reflection maxima							
1.5	1328.4	442.8	265.7	189.8	147.6	120.8	102.2	88.6
1.55	1374.1	458.0	274.8	196.3	152.7	124.9	105.7	91.6
1.6	1419.8	473.3	284.0	202.8	157.8	129.1	109.2	94.7
1.65	1465.5	488.5	293.1	209.4	162.8	133.2	112.7	97.7
1.7	1511.4	503.8	302.3	215.9	167.9	137.4	116.3	100.8
1.75	1557.3	519.1	311.5	222.5	173.0	141.6	119.8	103.8
1.8	1603.2	534.4	320.6	229.0	178.1	145.7	123.3	106.9
1.85	1649.2	549.7	329.8	235.6	183.2	149.9	126.9	109.9
1.9	1695.2	565.1	339.0	242.2	188.4	154.1	130.4	113.0
1.95	1741.3	580.4	348.3	248.8	193.5	158.3	133.9	116.1
2	1787.4	595.8	357.5	255.3	198.6	162.5	137.5	119.2
2.05	1833.5	611.2	366.7	261.9	203.7	166.7	141.0	122.2
2.1	1879.6	626.5	375.9	268.5	208.8	170.9	144.6	125.3
2.15	1925.8	641.9	385.2	275.1	214.0	175.1	148.1	128.4
2.2	1972.1	657.4	394.4	281.7	219.1	179.3	151.7	131.5
2.25	2018.3	672.8	403.7	288.3	224.3	183.5	155.3	134.6
2.3	2064.5	688.2	412.9	294.9	229.4	187.7	158.8	137.6
2.35	2110.8	703.6	422.2	301.5	234.5	191.9	162.4	140.7
2.4	2157.1	719.0	431.4	308.2	239.7	196.1	165.9	143.8
2.45	2203.5	734.5	440.7	314.8	244.8	200.3	169.5	146.9
2.5	2249.8	749.9	450.0	321.4	250.0	204.5	173.1	150.0
2.55	2296.1	765.4	459.2	328.0	255.1	208.7	176.6	153.1
2.6	2342.5	780.8	468.5	334.6	260.3	213.0	180.2	156.2
2.65	2388.9	796.3	477.8	341.3	265.4	217.2	183.8	159.3
2.7	2435.3	811.8	487.1	347.9	270.6	221.4	187.3	162.4
2.75	2481.7	827.2	496.3	354.5	275.7	225.6	190.9	165.4
2.8	2528.1	842.7	505.6	361.2	280.9	229.8	194.5	168.5
2.85	2574.6	858.2	514.9	367.8	286.1	234.1	198.0	171.6
2.9	2621.0	873.7	524.2	374.4	291.2	238.3	201.6	174.7
2.95	2667.5	889.2	533.5	381.1	296.4	242.5	205.2	177.8
3	2713.9	904.6	542.8	387.7	301.5	246.7	208.8	180.9
3.05	2760.4	920.1	552.1	394.3	306.7	250.9	212.3	184.0
3.1	2806.9	935.6	561.4	401.0	311.9	255.2	215.9	187.1
3.15	2853.4	951.1	570.7	407.6	317.0	259.4	219.5	190.2
3.2	2899.9	966.6	580.0	414.3	322.2	263.6	223.1	193.3
3.25	2946.4	982.1	589.3	420.9	327.4	267.9	226.6	196.4
3.3	2992.9	997.6	598.6	427.6	332.5	272.1	230.2	199.5
3.35	3039.4	1013.1	607.9	434.2	337.7	276.3	233.8	202.6
3.4	3086.0	1028.7	617.2	440.9	342.9	280.5	237.4	205.7
3.45	3132.5	1044.2	626.5	447.5	348.1	284.8	241.0	208.8
3.5	3179.1	1059.7	635.8	454.2	353.2	289.0	244.5	211.9
3.55	3225.6	1075.2	645.1	460.8	358.4	293.2	248.1	215.0
3.6	3272.2	1090.7	654.4	467.5	363.6	297.5	251.7	218.1
3.65	3318.7	1106.2	663.7	474.1	368.7	301.7	255.3	221.2
3.7	3365.3	1121.8	673.1	480.8	373.9	305.9	258.9	224.4
3.75	3411.9	1137.3	682.4	487.4	379.1	310.2	262.5	227.5
3.8	3458.4	1152.8	691.7	494.1	384.3	314.4	266.0	230.6
3.85	3505.0	1168.3	701.0	500.7	389.4	318.6	269.6	233.7
3.9	3551.6	1183.9	710.3	507.4	394.6	322.9	273.2	236.8
3.95	3598.2	1199.4	719.6	514.0	399.8	327.1	276.8	239.9
4	3644.8	1214.9	729.0	520.7	405.0	331.3	280.4	243.0

Table C-2: Wavelengths of Reflection Minima for Different Refractive Indices								
**Match the wavelength and fringe order				Sample Thickness(d) in (nm)				233.8
from collected data to table below				Incident Angle(in Radians)				0.349
Fringe#(m)	0	1	2	3	4	5	6	7
Index(n)	Wavelength in (nm) of the associated reflection maxima							
1.5	664.2	332.1	221.4	166.1	132.8	110.7	94.9	83.0
1.55	687.0	343.5	229.0	171.8	137.4	114.5	98.1	85.9
1.6	709.9	354.9	236.6	177.5	142.0	118.3	101.4	88.7
1.65	732.8	366.4	244.3	183.2	146.6	122.1	104.7	91.6
1.7	755.7	377.8	251.9	188.9	151.1	125.9	108.0	94.5
1.75	778.6	389.3	259.5	194.7	155.7	129.8	111.2	97.3
1.8	801.6	400.8	267.2	200.4	160.3	133.6	114.5	100.2
1.85	824.6	412.3	274.9	206.1	164.9	137.4	117.8	103.1
1.9	847.6	423.8	282.5	211.9	169.5	141.3	121.1	106.0
1.95	870.6	435.3	290.2	217.7	174.1	145.1	124.4	108.8
2	893.7	446.8	297.9	223.4	178.7	148.9	127.7	111.7
2.05	916.7	458.4	305.6	229.2	183.3	152.8	131.0	114.6
2.1	939.8	469.9	313.3	235.0	188.0	156.6	134.3	117.5
2.15	962.9	481.5	321.0	240.7	192.6	160.5	137.6	120.4
2.2	986.0	493.0	328.7	246.5	197.2	164.3	140.9	123.3
2.25	1009.1	504.6	336.4	252.3	201.8	168.2	144.2	126.1
2.3	1032.3	516.1	344.1	258.1	206.5	172.0	147.5	129.0
2.35	1055.4	527.7	351.8	263.9	211.1	175.9	150.8	131.9
2.4	1078.6	539.3	359.5	269.6	215.7	179.8	154.1	134.8
2.45	1101.7	550.9	367.2	275.4	220.3	183.6	157.4	137.7
2.5	1124.9	562.4	375.0	281.2	225.0	187.5	160.7	140.6
2.55	1148.1	574.0	382.7	287.0	229.6	191.3	164.0	143.5
2.6	1171.3	585.6	390.4	292.8	234.3	195.2	167.3	146.4
2.65	1194.4	597.2	398.1	298.6	238.9	199.1	170.6	149.3
2.7	1217.6	608.8	405.9	304.4	243.5	202.9	173.9	152.2
2.75	1240.9	620.4	413.6	310.2	248.2	206.8	177.3	155.1
2.8	1264.1	632.0	421.4	316.0	252.8	210.7	180.6	158.0
2.85	1287.3	643.6	429.1	321.8	257.5	214.5	183.9	160.9
2.9	1310.5	655.3	436.8	327.6	262.1	218.4	187.2	163.8
2.95	1333.7	666.9	444.6	333.4	266.7	222.3	190.5	166.7
3	1357.0	678.5	452.3	339.2	271.4	226.2	193.9	169.6
3.05	1380.2	690.1	460.1	345.1	276.0	230.0	197.2	172.5
3.1	1403.4	701.7	467.8	350.9	280.7	233.9	200.5	175.4
3.15	1426.7	713.3	475.6	356.7	285.3	237.8	203.8	178.3
3.2	1449.9	725.0	483.3	362.5	290.0	241.7	207.1	181.2
3.25	1473.2	736.6	491.1	368.3	294.6	245.5	210.5	184.1
3.3	1496.5	748.2	498.8	374.1	299.3	249.4	213.8	187.1
3.35	1519.7	759.9	506.6	379.9	303.9	253.3	217.1	190.0
3.4	1543.0	771.5	514.3	385.7	308.6	257.2	220.4	192.9
3.45	1566.3	783.1	522.1	391.6	313.3	261.0	223.8	195.8
3.5	1589.5	794.8	529.8	397.4	317.9	264.9	227.1	198.7
3.55	1612.8	806.4	537.6	403.2	322.6	268.8	230.4	201.6
3.6	1636.1	818.0	545.4	409.0	327.2	272.7	233.7	204.5
3.65	1659.4	829.7	553.1	414.8	331.9	276.6	237.1	207.4
3.7	1682.6	841.3	560.9	420.7	336.5	280.4	240.4	210.3
3.75	1705.9	853.0	568.6	426.5	341.2	284.3	243.7	213.2
3.8	1729.2	864.6	576.4	432.3	345.8	288.2	247.0	216.2
3.85	1752.5	876.3	584.2	438.1	350.5	292.1	250.4	219.1
3.9	1775.8	887.9	591.9	444.0	355.2	296.0	253.7	222.0
3.95	1799.1	899.5	599.7	449.8	359.8	299.8	257.0	224.9
4	1822.4	911.2	607.5	455.6	364.5	303.7	260.3	227.8

There are now nine data points, listed in Table C-3, that give a good indication of the magnitude and behavior of the wavelength dependent refractive index of the thin film sample. It is now a simple matter to derive a continuous functional representation of the refractive index using any mathematics software. The Maple code for doing so is depicted in Figure C-2 where the data points in Table C-3 are used in a least squares fit using Cauchy's formula. The resulting equation for the refractive index can then plotted in Maple (shown below) or copied into a spreadsheet program and used for further analysis of the reflectance and transmittance spectra.

Table C-3: Refractive Index

Wavelength (nm)	Index (n)
327	3.95
336	3.7
343	3.4
360	3.18
380	2.94
417	2.78
476	2.64
573	2.54
754	2.52

Figure C-2: Least Squares Fit to Data Using Maple 6 Software

```
> restart:with(plots):
Warning, the name changecoords has been redefined
> with(stats):
```

Least Squares fit to Cauchy's formula for the wavelength dependent refractive index:

```
> fit[leastsquare[[x,n], n=a/x^6+b/x^4+c/x^2+d]](
[[327,336,343,360,380,417,476,573,754],[3.95,3.7,3.4,3.18,2.9
4,2.78,2.64,2.54,2.52]]);
```

$$n = .5616865104\ 10^{16}\frac{1}{x^6} - \frac{.5890964142\ 10^{11}}{x^4} + \frac{242268.5013}{x^2} + 2.228839942$$

```
> n:=.5616865104e16*1/(x^6)-
.5890964142e11/(x^4)+242268.5013/(x^2)+2.228839942:
> plot(n,x=300..900,view=[300..900,2..4]);
```